Understanding the Role of Coordinatively Unsaturated Al^{3+} Sites on Nanoshaped Al_2O_3 for Creating Uniform Ni-Cu Alloys for Selective Hydrogenation of Acetylene

Yuanfei Song, [1] Shaoxia Weng, [1] Fan Xue,[2] Alan J. McCue,[3,]* Lirong Zheng[4], Yufei He, [1] Junting Feng, [1] Yanan Liu,[1,]* Dianqing Li[1,]*

[1]*State Key Laboratory of Chemical Resource Engineering, Beijing Engineering Center for Hierarchical Catalysts, Beijing University of Chemical Technology, Beijing, 100029, China*

[2] *Institute of Solid State Chemistry, University of Science and Technology Beijing, Beijing 100083, People's Republic of China*

[3] *Department of Chemistry, University of Aberdeen, Aberdeen AB24 3UE, U.K.*

[4] *High Energy Physics, Chinese Academy of Sciences, Beijing 100049, China*

* Corresponding author

Address: Box 98, 15 Bei San Huan East Road, Beijing 100029, China

Tel: +86 10 64436992 Fax: +86 10 64436992

E-mail address: a.mccue@abdn.ac.uk (Alan J. McCue); ynliu@mail.buct.edu.cn (Yanan Liu); lidq@mail.buct.edu.cn (Dianqing Li)

ABSTRACT

In this work, we report a synthesis approach for catalyst preparation by using shaped-controlled Al_2O_3 supports with enriched quantities of coordinatively unsaturated Al^{3+} centers. These centers can then induce ordering in bimetallic catalysts, even with a simple impregnation strategy and this is shown to be beneficial for selective hydrogenation of acetylene. Interestingly, nanorod Al_2O_3 induced a highly homogeneous and ordered Ni_1Cu_1 nanoalloy, mainly attributed to the coordination effect of unsaturated Al^{3+} sites that accelerate atomic diffusion and ordering (affirmed by molecular simulation). As-obtained Ni-Cu/Al_2O_3-rod catalyst exhibited both satisfactory activity and ethylene selectivity of 86% at mild reaction conditions which outperformed most of Ni-based catalysts reported to date. Through the combination of in situ DRIFTs studies and computational modeling by density functional theory, a di-

σ-adsorption mode of acetylene on the ordered Ni_1Cu_1 nanoalloy feature alternating rows of Cu and Ni atoms played a key role in the improvement of selectivity.

Keywords: Alumina; Support coordination induction; NiCu ordered alloy; Isolated Ni sties; Selective hydrogenation.

1. Introduction

Ethylene is one of the most vital petrochemicals with global demand in 2019 reaching 170 million tons. Of this, over 50% is then used for polymerization to produce polyethylene[1,2]. Approximately 75% of ethylene is produced by steam cracking of naphtha which also generates acetylene impurities that can irreversibly poison polymerization catalysts[3,4]. As a result of this, the modern polyethylene industry requires the content of acetylene in an ethylene feed to be less than 1 ppm[5]. Achieving high ethylene purity by means of chemical separation would account for an enormous amount of energy consumption. So instead, the selective hydrogenation of acetylene into ethylene is viewed as the most state-of-the-art strategy for purifying ethylene streams. This can be achieved commercially over supported Pd-based catalysts but these suffer from poor selectivity and high metal cost leading to the need for improved catalytic materials[6]. It is also noteworthy that since alkyne hydrogenation is a well-studied process, there is a wealth of literature to evaluate catalyst performance against.

Previous reports have suggested that a vinyl species is the key intermediate of acetylene hydrogenation that leads to selective formation to ethylene[7,8]. Therefore, to further improve acetylene hydrogenation catalysts, it is rational to design materials that possess a high-density of active sites with suitable adsorption strength for adsorbed hydrogen atoms (*H) and the vinyl intermediate. In principle, Ni metal with its incomplete d-electron orbital shows the ability to dissociate hydrogen[9] so could be used for acetylene hydrogenation. However, larger Ni ensembles may hinder ethylene formation because carbonic species bind strongly to continuous Ni sites in a multi-bridge configuration to generate an ethylidene intermediate[10], which can then be over-hydrogenated to obtain ethane or polymerized to generate 1,3-butadiene as the precursor of green oil (i.e., C_8^+ oligomers)[11,12]. Alternatively, the reactant acetylene

and/or the target product ethylene could decompose on the Ni surface to obtain a carbene species, which further polymerizes resulting in deposition of a harmful type of carbon species[13]. Consequently, for Ni to be effective for acetylene hydrogenation it would be preferably to construct formulations with discontinuous Ni sites (i.e., isolated Ni or Ni diluted/dispersed by another metal) that have been shown to facilitate the C_2H_2-to-C_2H_4 pathway[14,15]. Alloying with a second metal is feasible, although does not always lead to a uniform type of active site[16,17]. Indeed, a uniform or ordered alloy is far more beneficial for deriving structure-performance relationships[18]. A traditional impregnation strategy for catalyst preparation (as is preferred in industry) makes it difficult to synthesize ordered bimetallic alloy materials since the atomic ordering must overcome the kinetic energy barrier[19]. Consequently, high temperatures are generally required to accelerate atomic diffusion and ordering which promotes agglomeration, thus reducing the number of active sites[20]. This inspired us to explore a simply yet alternative method to fabricate ordered alloy catalysts.

Support materials with different surface coordination site are known to influence both the dispersion and electronic state of the active metal in monometallic catalysts[21]. However, the role of the support in the creation of bimetallic catalysts has received little attention to date with only a few reports. For instance, Divins et al.[22] reported that reducible cerium oxide could play an important role in controlling the surface rearrangement of bimetallic Rh-Pd nanoparticles. Similarly, Yang et al.[23] explored the influence of different supports (carbon, silica and titania) on the atomic-scale structure and chemical ordering of PdNiCo nanoalloys. Recently, our own experimental work[24] demonstrated that a metal-support interaction could influence the atomic arrangement of Ni-Cu nanoparticles. More specifically, when a support dominated by the CeO_2 (111) crystal plane was used, it could result in uniform and highly stable Ni-Cu nanoalloys even if a traditional impregnation method was adopted. The above work suggests that the formation of structured bimetallic particles can occur with a reducible oxide support, but this concept hasn't yet been explored deeply for more inert support materials.

Al_2O_3 is widely employed as a support in heterogeneous catalysis and this is especially true for the petroleum industry since Al_2O_3 is relatively inert and offers good

thermal stability. In the bulk of Al_2O_3, Al atoms exist in either a tetrahedral or octahedral coordination environment [25], whereas on the surface, coordinatively unsaturated Al^{3+} species appear, which can act as anchoring sites for active metals[26]. In this work, the role of these coordinatively unsaturated Al^{3+} sites were explored in detail by preparing a series of nanoshaped alumina which preferentially expose certain crystal facets. The supports were then used to prepare Ni-Cu catalysts via simple impregnation to explore the structural ordering of the resulting bimetallic catalysts. Detailed structural characterization revealed that the obtained Ni-Cu particles featured alternating rows of Cu and Ni atoms thus providing a high density of Ni-Cu pairs. This well-defined and stable Ni-Cu alloy was evaluated in the selective hydrogenation of acetylene and the catalytic mechanism was then explored by a range of techniques that suggested the ordering improved catalyst performance. As such, this report provides insight into how structured bimetallic catalysts may be produced by simple impregnation when fully utilizing the surface characteristics of a traditional catalyst support like Al_2O_3.

2. RESULT AND DISCUSSION

2.1. Characterization of pristine Al_2O_3

A series of nanoshaped Al_2O_3 crystals were fabricated by controlling the growth rate of specific crystal planes during the synthesis [27] – alumina nanorods, sheets and spindles are denoted as r-Al_2O_3, sh-Al_2O_3 and sp-Al_2O_3, respectively. The XRD patterns (see Figure 1A) show that Al_2O_3 nanocrystals are all composed of a well-crystallized gamma alumina phase with characteristic diffraction peaks at 2θ = 37.6, 39.5, 45.8 and 67.0°, which correspond to (311), (222), (400) and (440) crystal planes, respectively (JCPDS 10-0425). Notably, the peaks associated with the (311) and (222) planes are relatively weak, suggesting a disorder of the Al^{3+} species[28]. Besides the γ-Al_2O_3 peaks, there are no apparent impurities in sh- and r-Al_2O_3 samples, while an Al-O phase (solid aluminum suboxides, ICDD PDF 75-0278) possessing a cubic structure with the lattice constant of 5.67 Å inevitably appears in sp-Al_2O_3 due to the lattice relaxation of the (110) facet.[29,30] The morphology was explored by HRTEM analysis (Figure 1C-1E)

with good agreement between the observed nanocrystal shapes and lattice spacing relative to literature[27]. In detail, the sh-Al_2O_3 sample (Figure $1C_1$ and S1A) possesses a sheet-like structure (*ca.* 50 x 30 nm) which preferentially exposes the {111} facets as the large flat face. Within the image of Figure 1C some sheets appear to be sitting side on and have an apparent thickness of approximately 4 nm. The r-Al_2O_3 sample does indeed possess a rod-like structure with an average length of *ca.*180 nm and an average diameter of 10 nm but with a rougher surface (Figure 1E and S1C). Figure 1D presents a representative TEM image of the sp-Al_2O_3. As expected, the sample does possess a spindle like morphology – best described as being a rod like structure with convex shape along the longest dimension that equates to a gradual curvature of the surface. The spindle-shaped structures have an average length of ca. 100 nm and an average diameter of 18 nm. The structural model suggests the majority of the surface is best described as the {100} facet but the spindle also includes some {110} facets.

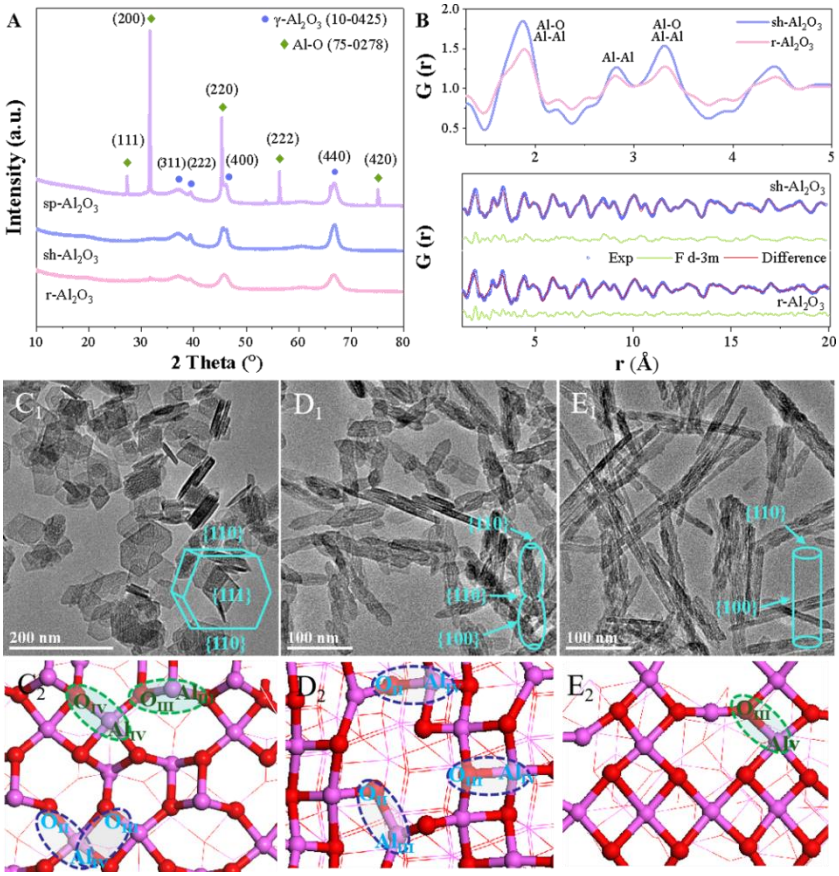

Figure 1 Structure of pristine nanoshaped Al_2O_3. (A) XRD patterns; (B) Pair Distribution Function (PDF) and the refinements using Fd-3m for r-Al_2O_3 and sh-Al_2O_3 (the experimental data are expressed by blue lines, while red ones are the calculated PDF patterns. The green lines are the

difference between the calculated results and the experimental data); HRTEM images and structure models of Al^{3+} coordination of ($C_{1\text{-}2}$) sh-Al_2O_3, ($D_{1\text{-}2}$) sp-Al_2O_3, ($E_{1\text{-}2}$) r-Al_2O_3 with schematic illustration of Al_2O_3 morphology inset.

High-resolution ^{27}Al solid state NMR spectra were collected at ultrahigh magnetic fields for the synthesized Al_2O_3 materials. As shown in Figure 3A, three distinct Al coordination environments are seen at chemical shifts of 7, 46, and 65 parts per million (ppm) relative to 1 mol L^{-1} aqueous $Al(NO_3)_3$. The peaks at 7 and 65 ppm are assigned to Al^{3+} species with octahedral and tetrahedral coordination, respectively, which correspond to the expected bulk phase Al species for an alumina.[26,28] The resonance at 46 ppm represents unsaturated Al^{3+} with a pentahedral coordination (see structure models of Al^{3+} coordination in Figure $1C_2$-E_2)[26], which are created on the Al_2O_3 surface by dehydration and dehydroxylation at elevated temperatures (≈ 500 ^oC). Based on peak fitting (see Table S1), the sh-Al_2O_3, r-Al_2O_3 and sp-Al_2O_3 samples synthesized in this work contain ca. 4.3%, 7.5% and 15.8% of these penta-coordinate Al^{3+} which can be crucial for anchoring metal ions. In order to further illustrate the different coordination structures of Al^{3+} species, Pair Distribution Function (PDF) characterization was carried out for sh-Al_2O_3 and r-Al_2O_3 as representative samples. In Figure 1B, typical PDF data are exhibited at distances of 1.3–5.0 Å. Note that the R_w factors fall within the acceptable region. Comparing with Al_2O_3 nanosheets, the peak intensity at 1.9 Å related to Al-O and the nearest Al-Al distance over r-Al_2O_3 decreases, while the second and third shell layers at 2.8 Å and 3.3 Å show the same trend, indicating lower coordination number of Al^{3+} species, consistent with the NMR result.

2.2. Structure of Al_2O_3 supported bimetallic Ni-Cu catalysts

It is generally accepted that coordinatively unsaturated Al^{3+} centers facilitate anchoring of metal atoms and in turn promote dispersion and thermal stability of metal nanoparticles.[26] However, detailed insight into the role of unsaturated Al^{3+} sites in bimetallic systems have not yet been reported. As such, this aspect is considered here by utilizing the series of nanoshaped alumina as supports for a bimetallic Ni-Cu catalyst

using a traditional impregnation method (samples use the same coding as the supports but contain the prefix 'Ni-Cu' to denote metal addition). The metal loadings of all the catalysts were determined by elemental analysis (Table S2) are slightly lower than the nominal loading, however, all 3 samples have broadly similar metal loadings and a Ni/Cu atomic ratio close to 1 as intended. As such, differences in catalytic performance (see later) are thought to be related to the distribution of the two metals as opposed differences in metal loading. Investigation by STEM (Figure 2A_1-C_1) suggest the Ni-Cu particle size follows the sequence: r-Al_2O_3 (5.6 nm) < sh-Al_2O_3 (7.5 nm) < sp-Al_2O_3 (11.3 nm), with the dispersion having the opposite trend. In general (and as reported elsewhere),[31] the metal particle size could be linked to the surface area of support materials. However, in our case, the surface area alone cannot explain the trend in particle size (sh-Al_2O_3 has smaller particle size but with lower surface area than that of sp-Al_2O_3; Figure S2 and Table S3), suggesting other support properties may play a role.

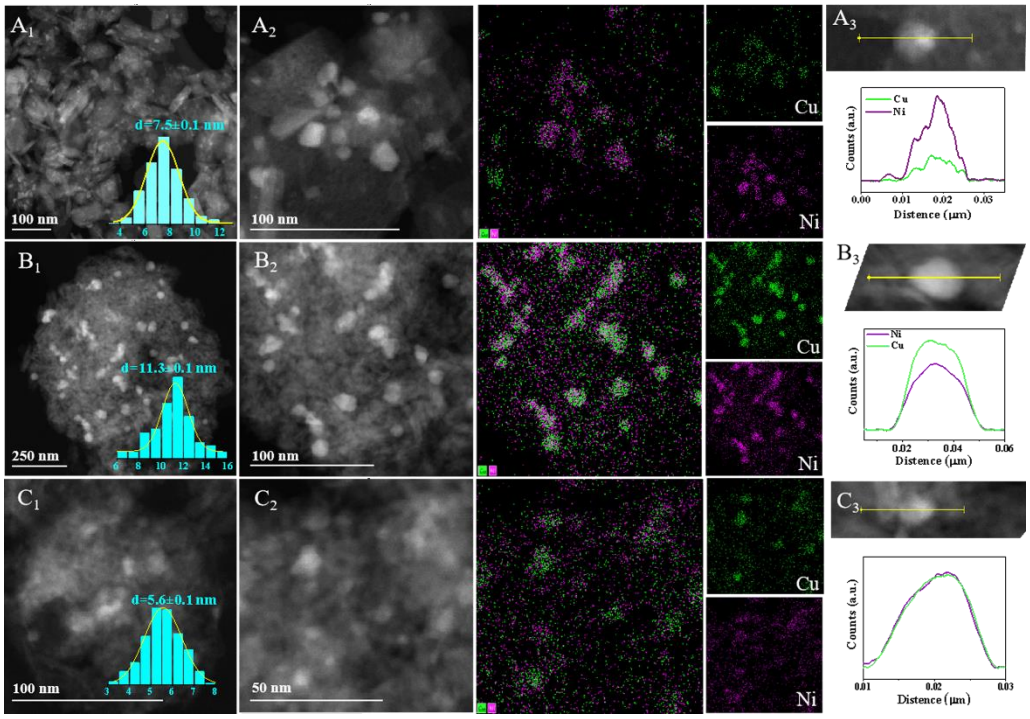

Figure 2 Dispersion and geometric structure over Ni-Cu/Al_2O_3 catalysts. STEM images with the particle distribution, elemental mappings and line scanning of (A_{1-3}) Ni-Cu/sh-Al_2O_3; (B_{1-3}) Ni-Cu/sp-Al_2O_3; (C_{1-3}) Ni-Cu/r-Al_2O_3.

Notably, the addition of Ni and Cu results in a decrease in the number of penta-coordinated Al^{3+} sites as judged by SS-NMR (Figure 3B and Table S1) and this is accompanied by an increase in the 7-ppm feature. This is considered as evidence that the penta-coordinated Al^{3+} centers are important anchoring sites for Ni and Cu atoms. The effect is most pronounced for the Ni-Cu/r-Al_2O_3 sample which also appears consistent with our interpretation. However, for sp-Al_2O_3 with more pentacoordinate Al^{3+} sites and a larger specific surface area than that of sh-Al_2O_3, the particle size of Ni-Cu/sp-Al_2O_3 is larger than Ni-Cu/sh-Al_2O_3 catalysts, which is likely related to the presence of some pores with smaller pore diameter in sp-Al_2O_3 (Figure S2), which leads to a degree of pore entrance blocking[32,33], thus decreasing the metal dispersion.

Through detailed STEM/EDX analysis it is also possible to gain insight into how the two metals mix/alloy. For all three samples, there is a correlation between where the two metals are present on the support (see Figure $2A_{2\text{-}3}$-$C_{2\text{-}3}$). More interestingly, it is found that the r-Al_2O_3 supported bimetallic catalyst displays a highly ordered alloy. STEM mapping suggests a homogeneous distribution of Cu and Ni at the nanoscale (Figure 2C) with a Ni/Cu ratio of 51:49 and this is in agreement with XRD results (Figure S3) that confirm the presence of a Ni_1Cu_1 phase. The Ni-Cu/sp-Al_2O_3 sample also appears to show alloyed Ni and Cu, although the distribution may be more complex. XRD suggests a Ni-Cu alloy phase may exist, but STEM elemental mapping suggests alloying with Cu enrichment on the surface (Figure 2B). For the Ni-Cu/sh-Al_2O_3 catalyst, there is evidence that both monometallic Cu and Ni-rich bimetallic nanoparticles co-exist and this will have an impact on catalytic properties (Figure 2A). This data appears to match with TPR analysis as well (Figure S4), where a reduction peak emerges at 230 °C for Ni-Cu/r-Al_2O_3, which is lower than other samples owing to the existence of the uniform NiCu nanoalloy[34]. CO-FTIR was further employed to characterize the samples. Initially, the spectra of the samples were collected prior to purging of gas phase CO as shown in Figure S5. The peak at ca. 2130 cm^{-1} is assigned to CO binding to Cu surface atoms[35], while the additional peaks at 2170, 2110 and 2057 cm^{-1} are related to the gas phase CO and Ni carbonyls[36]. Notably, Ni-Cu/r-Al_2O_3 exhibits a relatively weak band associated with adsorption of CO on Cu, with this

characteristic band being more apparent for Ni-Cu/sh-Al_2O_3 and Ni-Cu/sp-Al_2O_3 samples. This is consistent with either Cu surface enrichment or some monometallic Cu particles which generally correlates with STEM analysis (see earlier). Samples were then subjected to Ar purging of increasing durations such that the gas phase CO was removed (Figure S5). This also tends to result in loss of CO adsorbed on Cu. The spectra after Ar purging are shown in Figure 3C. The sample prepared on the sheet alumina shows an absorption band in the Ni bridge bound region of 2000-1800 cm^{-1}. The spectrum of Ni-Cu/sp-Al_2O_3 shows that two relatively weak bands are observed at 1963 and 1826 cm^{-1} which correspond to CO bridge-bound on Ni ensembles with a small amount of linear bound CO at 2016 cm^{-1} on Ni^0 [37,38]. This implies that whilst alloying with Cu could reduce Ni-Ni nearest neighboring, some larger Ni ensembles still exist in Ni-Cu/sp-Al_2O_3 although both XRD and STEM elemental mapping results suggest the formation of a Ni-Cu alloy phase. The phenomena may be ascribed to the random arrangement of Ni and Cu atoms, leading to incomplete isolation of Ni atoms or some regions of continuous Ni sites – in other words the sample is characterized as a disordered alloy. As expected, CO molecules only appear linearly absorbed on Ni atoms in the Ni-Cu/r-Al_2O_3 sample without any bridge bound absorption peaks. Whilst this level of analysis does indicate that the catalyst materials are complex it does show that control of the support morphology can influence bimetallic particle formation, even with a simple impregnation strategy.

The coordination environment was further analyzed using Ni K-edge EXAFS as shown in Figure 3D. The first nearest neighbor distance in Ni–Cu nanoparticle increases to high R value compared with that in Ni foil: Ni < Ni-Cu/sh-Al_2O_3 < Ni-Cu/sp-Al_2O_3 < Ni-Cu/r-Al_2O_3, which indicates a strong Ni–Cu interaction through chemical bonding.[39] The curve fitting results of these samples are listed in Figure S6 and Table S4. A peak at ca. 2.48 Å corresponds to Ni-Ni interaction of the reference Ni foil.[40] Noticeably, the neighboring distance increases to a higher R value of 2.51 Å for Ni-Cu/sp-Al_2O_3 sample, suggesting the presence of the aforementioned Ni-Cu alloy. This effect is most apparent for Ni-Cu/r-Al_2O_3 sample (2.54 Å) which is consistent with STEM analysis. Moreover, the decreased coordination number of Ni–Cu catalysts

relative to that of Ni foil (12) indicates the interspersion of Ni and Cu elements, in which Ni-Cu/r-Al_2O_3 exhibits the smallest coordination number of Ni-Ni as the unique structural feature of the uniform alloy.[41]

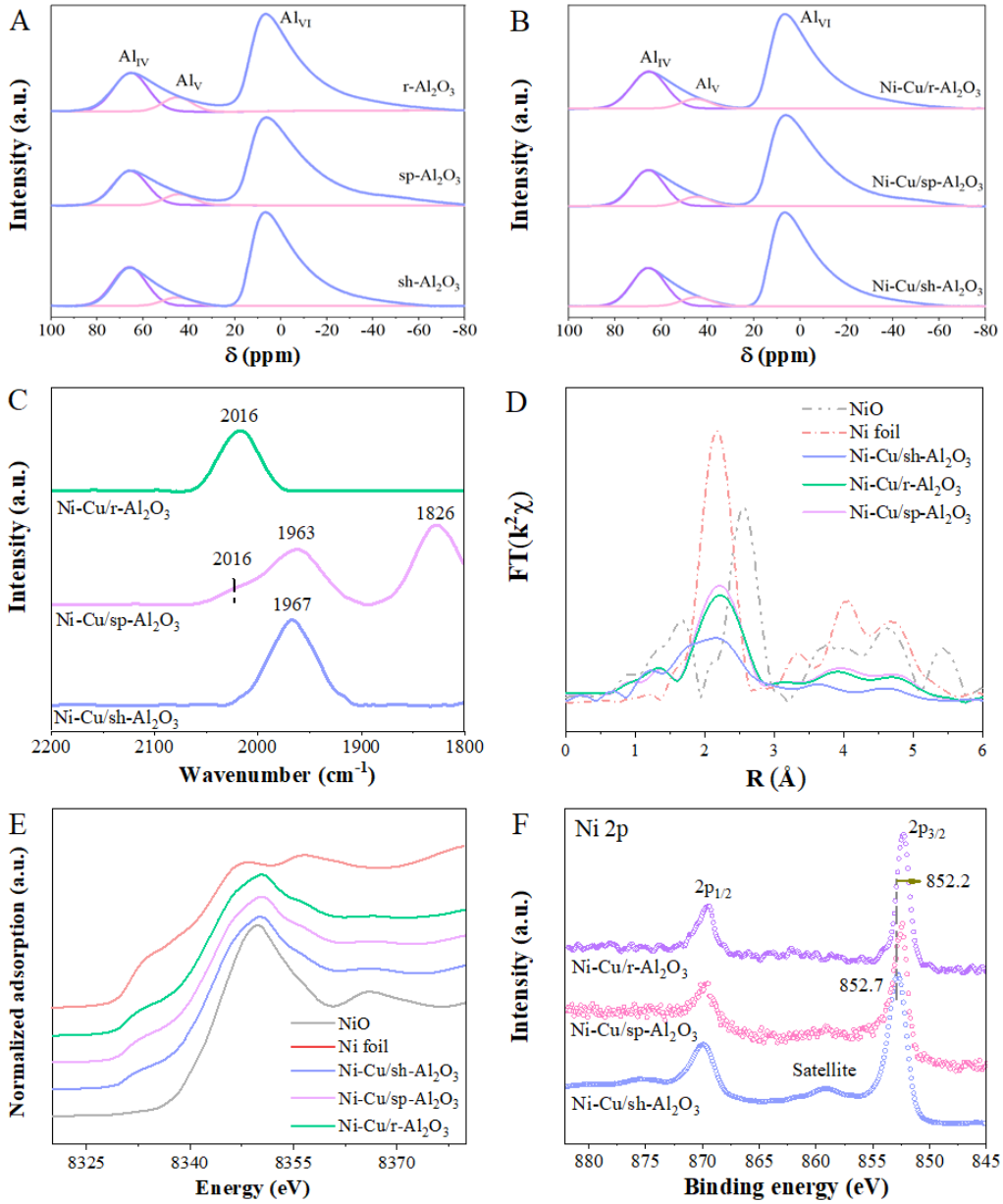

Figure 3 Fine structure of Ni-Cu/Al_2O_3 catalysts. ^{27}Al NMR spectra of (A) Al_2O_3 (B) Ni-Cu catalysts; (C) CO-FTIR spectra; (D) Fourier transform k^2-weighted Ni K-edge EXAFS spectra; (E) Normalized XANES spectra with NiO and Ni foil as the references; (F) In situ XPS spectra of Ni 2p for Ni-Cu/sh-Al_2O_3, Ni-Cu/sp-Al_2O_3 and Ni-Cu/r-Al_2O_3

The spectra of Ni-Cu/sp-Al_2O_3 samples looks largely similar with that of Ni-Cu/r-Al_2O_3 but with higher coordination number, showing that this catalyst possesses a

similar alloy structure but the interspersion degree of Ni and Cu elements is lower; that is to say, Ni ensembles may still exist in Ni-Cu/sp-Al_2O_3 which would be consistent with STEM data. However, the largest difference is for Ni-Cu/sh-Al_2O_3 sample, which shows a far broader peak in this region perhaps suggesting a more mixed first coordination sphere around Ni atoms – possibly associated with a metal oxide. This could be ascribed to a structure with both monometallic Cu and Ni-rich bimetallic nanoparticles co-existing in Ni-Cu/sh-Al_2O_3, leading to the weak interaction between Ni and Cu, and thus easier oxidation. Similarly, as shown in Figure S7, Fourier-transformed Cu k-edge EXAFS spectra show that show that only a small contribution of Cu−O bond to the spectra of Ni-Cu/r-Al_2O_3 is suggested with more metallic state in comparison with those of Ni-Cu/sp-Al_2O_3 and Ni-Cu/sh-Al_2O_3 samples. However, no feature of a Cu-Cu shell from CuO is observed, indicating that the CuO species are insignificant. The Cu k-edge EXAFS curve-fitting parameters are summarized in Table S5. The metal-metal bond length for Cu in Ni-Cu/r-Al_2O_3 is close to the intermediate value (2.51 Å) between Ni foil (2.48 Å) and Cu foil (2.54 Å) which is consistent with the information obtained from the Ni k-edge XAS results – so again this infers the formation of a uniform Ni_1Cu_1 alloy[42]. No apparent difference in the coordination numbers is observed for Cu−Cu/Ni and Ni−Ni/Cu shells (5.7 and 5.9, respectively), supporting homogeneous alloying in this sample. Notably, Ni-Cu/sp-Al_2O_3 and Ni-Cu/sh-Al_2O_3 catalysts possess an atomic distance of 2.53-2.54 Å, which is close to Cu foil, suggesting that the existence of either Cu surface enrichment or some monometallic Cu particles is likely, in agreement with STEM analysis. Meanwhile, the coordination numbers of Cu−O shell in these two catalysts are 2.2 and 2.8, indicating the existence of a large amount of Cu oxide species due to the weak interaction between Ni and Cu atoms without the formation of homogeneous alloy structure. The apparent variation of the structure in Ni-Cu nanoparticles over different Al_2O_3 support when employing the same impregnation route indicates the nature of support, specifically coordination structure could play an important role in the atomic arrangement of metal components.

Figure 3E shows X-ray Absorption Near-Edge Structure (XANES) spectra of Ni-Cu/Al_2O_3 samples including Ni foil and NiO as reference. The near-edge line in Ni-Cu materials is similar to Ni foil, while the intensity of white line increases slightly,[43] indicating the Ni species is mainly retained in the metallic during this ex-situ testing. Similar phenomena are also observed in Cu k-edges XANES spectra (Figure S8). XPS analysis was employed to explore the electronic state of Ni and Cu on nanoshaped alumina. Prior to analysis, samples were in-situ reduced to ensure that the analysis was of the metals in a reduced state (i.e., analogous to catalytic tests – see later). In the Ni 2p region (shown in Figure 3F), two peaks are generally observed – $2p_{3/2}$ at approx. 852-853 eV and the $2p_{1/2}$ at 869-970 eV. For the Ni-Cu/sh-Al_2O_3 sample, these peaks appear at 852.7 and 869.9 eV with the binding energy (BE) typical of a Ni^0 species.[44] The equivalent peaks for the spindle and rod samples shift to lower BE suggesting a degree of electron transfer from Cu to Ni.[45] Furthermore, the extent of this shift seems to correlate with alloying degree (i.e., Ni-Cu/r-Al_2O_3 has the lowest BE (852.2 eV) but is the most ordered alloy). Note that this is consistent with Cu 2p results (Figure S9), where the Cu $2p_{3/2}$ peak shifts to higher energy suggesting a Cu species that is electron deficient in Ni-Cu/r-Al_2O_3.

It is clear that the nanorod Al_2O_3 supported Ni-Cu catalyst possesses a more uniform alloy structure than the nanosheet or nanospindle support – the key question therefore becomes why? To explore this, molecular simulations were carried out to gain insight into the nature of the interactions between the unsaturated Al^{3+} centers and active metals during synthesis. Using the material studio, an initial structure model of gamma alumina with the (100) facet was established (Figure S10), which shows that a penta-coordinated Al^{3+} species exists on the surface of Al_2O_3, while tetra- and hexa-coordination environment exist within the cell structure. In contrast, a conventional Al_2O_3 with only a small amount Al_V^{3+} sites were chosen for comparison (Figure S11). By tracing the trajectories of two Ni and two Cu atoms as they approach the surface the initial surface anchoring of the metal atoms could be followed (Figure S12-S13). It is interesting to note that Ni and Cu atoms appear to simultaneously nucleate/bind to the same unsaturated Al_V^{3+} sites which forms the foundation of the well-arranged Ni-Cu

alloys (Figure S12). However, on a surface with a lower concentration of Al_V^{3+} species, Ni and Cu atoms are trapped by different Al^{3+} species leading to a less ordered alloy or even monometallic clusters (Figure S13). The results described above confirm that the structure of Ni-Cu nanoparticles is strongly influenced by interaction with penta-coordinated Al^{3+} centers. A higher surface concentration of such sites leads to the formation of a more ordered alloy. It therefore seems feasible to make use of this phenomenon in catalyst design. To demonstrate that this concept could be extended beyond transition groups metals, Ni-Sn samples were also briefly explored (Figure S14) with evidence of a uniform Ni-Sn alloy observed for the r-Al_2O_3 sample (note: in this system Sn can bond with Al_2O_3 support to form a tin-aluminate or migrate to the surface of Ni-Sn ensembles to reduce surface free energy meaning this system should be more fully investigated in future).[46]

2.3. Catalytic behavior for selective acetylene hydrogenation

Selective acetylene hydrogenation was used as a test reaction to explore the performance of the series of Ni-Cu/Al_2O_3 catalysts. Figure 4A shows the acetylene conversion as a function of temperature for all nanoshaped catalysts along with a sample prepared on commercial Al_2O_3 as reference (denoted as Ni-Cu/c-Al_2O_3). In the absence of any metal, the nanoshaped alumina show no catalytic activity (Figure S15). In contrast, nanoshaped Al_2O_3 supported bimetallic samples all exhibit catalytic activity with a relatively mild operating temperature window beginning around room temperature. The required temperature to achieve full conversion followed the sequence: Ni-Cu/sh-Al_2O_3 (70^{o}C) < Ni-Cu/sp-Al_2O_3 (80^{o}C) < Ni-Cu/c-Al_2O_3 (110^{o}C) < Ni-Cu/r-Al_2O_3 (130^{o}C). The acetylene hydrogenation reaction is a structure-sensitive reaction, with smaller metal particle size known to improve the catalytic activity[47]. As well known, the selective acetylene hydrogenation is a structure-sensitive reaction, with smaller metal particle size facilitating to improve the catalytic activity. Indeed, in our system, the order of catalytic activity is Ni-Cu/sh-Al_2O_3 > Ni-Cu/sp-Al_2O_3 with the opposed order in average particle size. That is to say, smaller particle size promotes the enhancement of activity. However, Ni-Cu/r-Al_2O_3 exhibits lower catalytic activity but

with the smallest particle size, which is abnormal phenomenon relative to the size effect. Consequently, this difference in the average size of Ni-Cu particles cannot be considered as the only reason for the disparity in the catalytic performance observed in this situation. As such, the relationship between structure and catalytic behavior will be further explore, which could be linked to the different atomic arrangement of Ni and Cu induced by Al_2O_3 support (see later). Furthermore, the apparent activation energies (E_a) were obtained from a plot of ln (TOF) versus 1/T (Figure 4C) – where TOF was assessed at low conversion (<15%) to rule out the effects of mass or heat transfer. When compared with the commercial Al_2O_3 sample, the E_a values of nanoshaped catalysts are all lower than the commercial alumina sample but otherwise similar to each other.

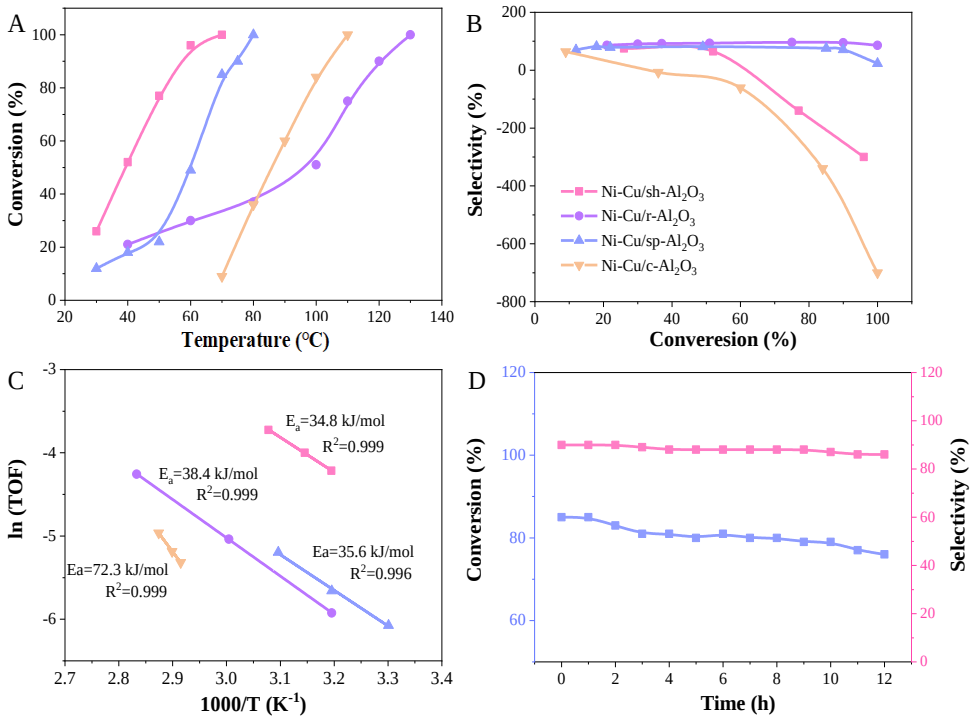

Figure 4 Catalytic behavior in the selective acetylene hydrogenation. (A) Acetylene conversion as a function of temperature; (B) ethylene selectivity as a function of acetylene conversion (reaction conditions: 0.3 g of catalyst, 10:1 of H_2/C_2H_2 ratio, total flow = 163 mL min^{-1}, SV = 9780 h^{-1}, the temperature in the range of 30-130 °C); (C) Arrhenius plots of Ni-Cu catalysts (D) Long-term stability for Ni-Cu/r-Al_2O_3 at 115 °C for 12 h.

In terms of selectivity, several points can be extracted from Figure 4B, S16 and S17. Firstly, Ni-Cu/r-Al_2O_3 sample exhibits the supreme ethylene selectivity with relatively

little ethane and oligomer formation, and this remains true at high acetylene conversion. Even at complete acetylene conversion (where over-hydrogenation will most readily occur) ethylene selectivity remains above 86.0% with 12.2% of ethane and 1.8% of oligomer as by-products, which is better than the monometallic Ni and Cu supported on r-Al_2O_3 (Figure S17) as well as that reported for most non-noble metal catalysts in literature (see Table S6). Secondly, both Ni-Cu/sh-Al_2O_3 and Ni-Cu/c-Al_2O_3 catalysts show a sharp drop in selectivity to negative values after complete conversion of acetylene, which doesn't occur for Ni-Cu/r-Al_2O_3 samples (note: a negative selectivity implies that a portion of ethylene presented in the feed undergoes hydrogenation to generate ethane and oligomers). This behavior is typical for a monometallic Ni catalyst or one with contiguous Ni ensembles (Figure S17). In terms of selectivity at full conversion, there appears to be a correlation with the uniformity of alloying or isolation degree of Ni atoms (i.e., Ni-Cu/c-Al_2O_3 < Ni-Cu/sh-Al_2O_3 < Ni-Cu/sp-Al_2O_3 < Ni-Cu/r-Al_2O_3). This suggests that the ordered NiCu alloys that preferentially form on the nanoshaped supports can facilitate the selective conversion of acetylene into ethylene. The stability of the best performing material, namely Ni-Cu/r-Al_2O_3, was further evaluated at 115 ^oC for a 12 h period (Figure 4D). Over this time period the conversion appears to decrease marginally but with no apparent shift in ethylene selectivity (≈ 90% throughout). Analysis of this catalyst after use shows no evidence of metal particle agglomeration (Figure S18) but a small amount of weight loss is observed by TGA consistent with some carbon retention (see Figure S19), responsible for the inconspicuous decrease of activity. However, for both Ni-Cu/sp-Al_2O_3 and Ni-Cu/sh-Al_2O_3 samples (Figure S20), it is found that there is an apparent decrease in selectivity for Ni-Cu/sp-Al_2O_3 (from 83.0% to 53.3%) after 7 h on stream and Ni-Cu/sh-Al_2O_3 (from 59.2% to negative) after only 4 h on stream. This is attributed to the presence of Ni or Cu ensembles (either within the alloy particles or as monometallic particles) which are known to favor oligomer formation leading to carbon build up. The detrimental carbonaceous species result in the coverage of active metal atoms and possibly pore blockage, which limits not only the access of hydrogen and acetylene to

the active sites but also the escape of ethylene into the gas stream and hence more deactivation is observed[2,10,48].

2.4. Insight into effects of Ni-Cu structure on catalytic behavior

It is generally accepted that the charge density and isolation degree of active species can significantly affect the binding strength of adsorbates or intermediates, which often accounts for the efficient and selective catalysis.[49] As discussed above, the orderly arrangement of Ni and Cu causes an increase of Ni electron density, which theoretically promotes ethylene desorption. To further probe this, *in-situ* DRIFTS experiments were performed with propyne as probe molecule at different reaction temperatures since acetylene does not give rise to particularly strong IR bands due to its symmetry. Taking the Ni-Cu/r-Al_2O_3 catalyst as an example (Figure 5A), the characteristic peaks in the ranges of 3200-3380, 2900-3000 and 2110-2160 cm^{-1} can be observed after propyne adsorption and correspond to unsaturated C-H, C-C vibrations in H-C≡C, and saturated C-H vibrations in -CH_3, respectively.[50] After addition of H_2 flow, two new peaks emerge at 1642 and 1121 cm^{-1} that are associated with C=C vibrations in H-C=C[51] which is consistent with conversion of alkyne into alkene. Similarly, for Ni-Cu/sh-Al_2O_3 (Figure 5B) and Ni-Cu/sp-Al_2O_3 (Figure 5C), a relatively weak peak at 1642 cm^{-1} is observed. However, as reaction temperature increased and/or reaction time was prolonged, the intensity of this peak decreases before disappearing entirely. Instead, a new shoulder appears at 1350 cm^{-1} for Ni-Cu/sh-Al_2O_3 (Figure 5B) which is ascribed to a C-H bending vibration implying conversion of alkyne into alkane.[52] Notably, the spectra of a propyne and H_2 mixture (Figure S21) is basically in agreement with that of pure propyne without the characteristic bands originating from the reaction intermediates and products since the reaction is not obviously driven at the room temperature. Moreover, to mimic real reaction conditions, DRIFT experiment with a flow of C_2H_2 and H_2 mixture was performed. Figure S22 presents the spectra collected during the hydrogenation of acetylene over Ni-Cu catalysts in the temperature range of 30-120 °C. Although the intensity of absorption bands is relatively weak, some information can still be extracted. The generation of ethylene on Ni-Cu/r-Al_2O_3

catalysts is affirmed by the appearance of the CH_2 scission and C=C stretching vibration at 1626 and 1709 cm^{-1}, respectively[53]. Notably, the characteristic bands assigned to -CH_3 asymmetric stretching of alkanes (2980 cm^{-1}) and -CH_2 asymmetric stretching of long-chain hydrocarbons (2925 cm^{-1}) are very weak suggesting little ethane or oligomer formation over Ni-Cu/r-Al_2O_3 catalyst. Furthermore, the band intensity corresponding to ethylene decreases with increasing temperature, indicating weak ethylene adsorption on Ni-Cu/r-Al_2O_3 surface. However, for Ni-Cu/sp-Al_2O_3 and Ni-Cu/sh-Al_2O_3 samples, although the ethylene is also formed, the intensity attenuates more gradually with increasing temperature. Meanwhile, the peaks at 2925 and 2980 cm^{-1} ascribed to longer chain hydrocarbons and ethane emerge. These observations would appear to correlate well with catalyst tests where continuous Ni sites in Ni-Cu/sp-Al_2O_3 and Ni-Cu/sh-Al_2O_3 hinder catalytic performance.

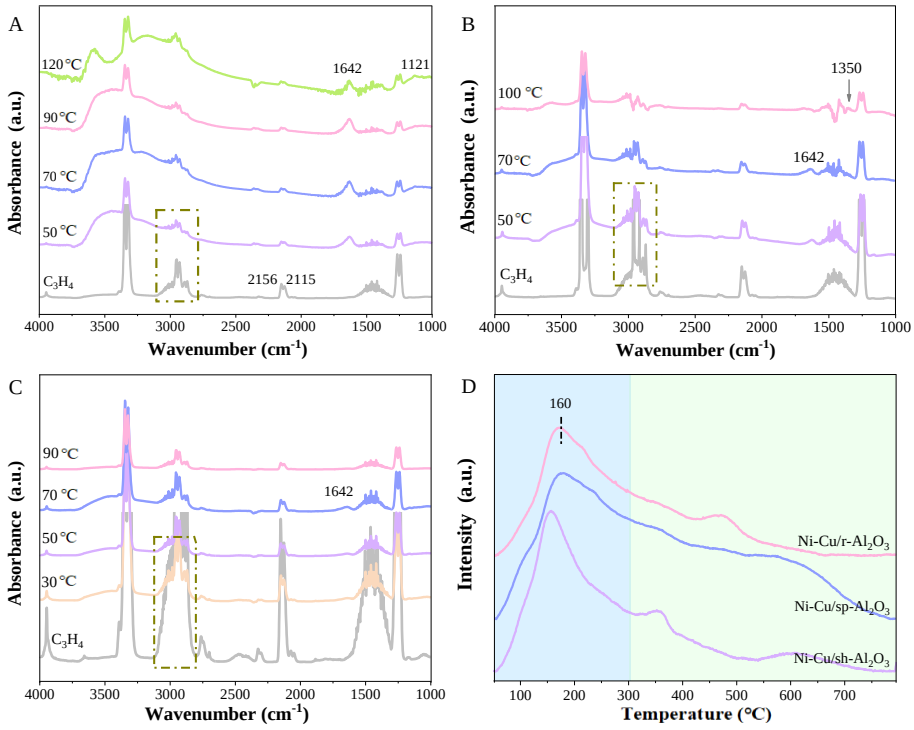

Figure 5 Study of structure-performance relationship. (A-C) In situ DRIFT spectra of propyne and a propyne/hydrogen mixture heated to different temperatures on (A) Ni-Cu/r-Al_2O_3, (B) Ni-Cu/sh-Al_2O_3; (C) Ni-Cu/sp-Al_2O_3; (D) C_2H_4-TPD profiles of Ni-Cu catalysts.

To explore how the ethylene desorption behavior changes between samples, we performed C_2H_4-TPD experiments. From the profiles in Figure 5D, two key regions

could be detected at 100-300 °C and 300-600 °C. The low temperature peak is the main desorption peak and originates from weak adsorption of ethylene in a di-σ configuration.[54] As this species is only weakly bound to the metal surface it should desorb fairly easily without over-hydrogenation or dissociation. The peak in the 300-600°C region is assigned to a multiply coordinated ethylene species[55] which can react more easily with dissociated H to produce ethane since it is adsorbed more strongly. With regard to Ni-Cu/sh-Al_2O_3 and Ni-Cu/sp-Al_2O_3 samples, the peak area associated with multiply coordinated ethylene is far greater than for Ni-Cu/r-Al_2O_3 catalyst. Furthermore, the peak position for multiply coordinated ethylene species shifts to higher temperature for the less selective catalysts. These phenomena collectively show that ethylene species can more easily desorb from the nanorod supported catalyst which correlates with lesser ethane formation.

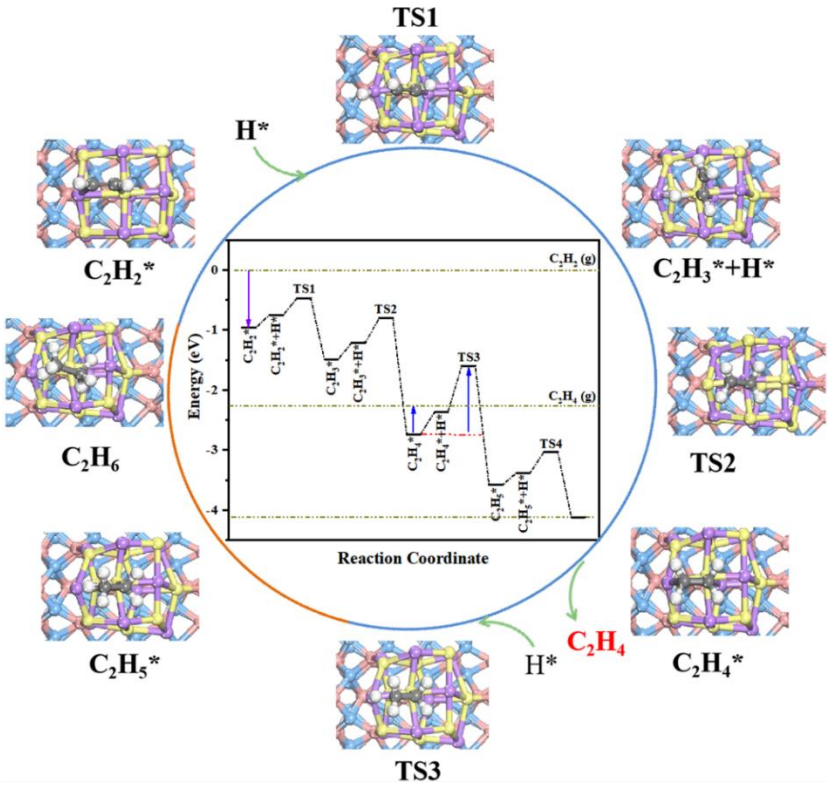

Figure 6. DFT calculation of optimized reaction path in acetylene hydrogenation for an ordered Ni_1Cu_1 alloy catalyst. The arrows mean the direction of the reaction, in which the blue and orange lines are the main and side reactions (grey: C atom; white: H atom; yellow: Ni atom; purple: Cu atom; pink: O atom; blue: Al atom).

DFT calculations were further conducted to probe the reaction mechanism on the well-ordered Ni-Cu alloy. A structural model related to the Ni-Cu/r-Al_2O_3 catalyst was constructed according to the experimental results (Figure S23), while the calculated potential energies, the adsorption configuration and free energies for acetylene hydrogenation are shown in Figures 6, S24 and S25. The acetylene molecule is seen to adsorb on Ni and the adjacent Cu atoms in di-σ-complex manner with adsorption energy of −0.96 eV. The reaction then proceeds through two-step successive hydrogenation steps (TS1 & TS2) to produce ethylene via a C_2H_3* intermediate.[56] The desorption energy of the adsorbed ethylene species is 0.46 eV, whereas the barrier for over-hydrogenation of form ethane is 0.77 eV (TS3). Given the relative size of these two barriers, it is more energetically favorable for ethylene to desorb and thus the Ni-Cu surface with isolated Ni atoms (i.e., no Ni-Ni nearest neighbors) leads to selective hydrogenation.[57] For comparison, on a Ni catalyst acetylene tends to adsorb on Ni ensembles in the three-fold bridge coordination[9] which leads to an adsorbed configuration with higher desorption energy resulting in lower ethylene selectivity.

3. Conclusion

In summary, we developed an effective strategy to construct highly homogeneous and ordered alloys induced by the support coordination structure. Specifically, a series of shaped Al_2O_3 supports with different contents of penta-coordinated Al^{3+} sites were fabricated as substrates to support non-noble metal Ni-Cu nanoparticles by conventional impregnation. Confirmed by the combination of EXAFS and STEM, the support surface was shown to influence the arrangement of metals within bimetallic particles. Nanospindle Al_2O_3 predominantly showed alloyed Ni and Cu particles but with Cu enrichment on the surface, while nanosheet Al_2O_3 triggered the formation of monometallic Cu and Ni-rich bimetallic nanoparticles. Interestingly, a well-dispersed and ordered Ni_1Cu_1 nanoalloy was observed on nanorod Al_2O_3 and molecular simulations showed that coordinatively unsaturated Al^{3+} centers provided a crucial role in the formation of metal nanoparticles where the Ni atoms were uniformly spaced by Cu atoms. By evaluating performance in the selective hydrogenation of acetylene, this

same uniformly structured Ni-Cu alloy with isolated Ni sites exhibited 86% ethylene selectivity at a conversion of 100% at a relatively mild reaction temperature of 130 °C with performance far exceeding that of catalysts with contiguous Ni ensembles. More importantly, excellent long-term stability was obtained with no evidence of deactivation via Ni atom aggregation with only minor coking during a 12 h time on stream. The excellent performance was attributed to the uniform metal particle structure which effectively isolated Ni sites whilst creating an electronic environment that favored ethylene desorption, thus improving ethylene selectivity. The underlying Ni_1Cu_1 structure is thought to be a direct consequence of the Al^{3+} centers on the surface of the Al_2O_3 support.

AUTHOR INFORMATION

Author Contributions

Yuanfei Song carried out most of the characterization, structural analysis, and catalytic reactions. Yanan Liu, Junting Feng, Yufei He and Dianqing Li designed the experiment and provided the funding support. Fan Xue performed the PDF analysis. Lirong Zheng conducted XAFS experiments. Yanan Liu and Alan J. McCue discussed the results and wrote the manuscript.

Notes

The authors declare no competing financial interest.

ASSOCIATED CONTENT

Supporting Information

The supporting information is available free of charge at https.

Details include experiment details/methods; HRTEM images, surface area, pore volume, size and catalytic performance of supports; XRD patterns; TPR profiles, Ni and Cu K-edge XAS spectra, Cu 2p XPS spectra of Ni-Cu catalysts; Structures model of supports and possible position for the anchoring of Ni and Cu atoms from molecular simulations; XRD profiles of Ni-Sn catalysts; Ethane selectivity and oligomer selectivity as a function of acetylene conversion for bimetallic Ni-Cu, monometallic Ni

and Cu catalysts; Longer-term stability; In situ DRIFT spectra of alkyne hydrogenation; Comparison of catalytic performance with literatures; HRTEM images and TG-MS analysis of spent Ni-Cu/r-Al_2O_3 catalysts; Gibbs free energy diagrams for acetylene hydrogenation.

ACKNOWLEDGMENTS

This work was financially supported by National Natural Science Foundation of China (22218017), National Key R&D Program of China (2021YFB3801600), and the Fundamental Research Funds for the Central Universities (buctrc201921, JD2223). We acknowledge the Beijing Synchrotron Radiation Facility (BSRF) for providing the experimental resources for XAS experiments.

References

[1] Zhang, L.; Zhou, M.; Wang, A.; Zhang, T. Selective Hydrogenation over Supported Metal Catalysts: From Nanoparticles to Single Atoms. *Chem. Rev.* **2020**, *120*, 683–733.

[2] Kuhn, M.; Lucas, M.; Claus, P. Long-Time Stability vs Deactivation of Pd-Ag/Al_2O_3 Egg-Shell Catalysts in Selective Hydrogenation of Acetylene. *Ind. Eng. Chem. Res.* **2015**, *54*, 6683−6691.

[3] Chai, Y.; Han, X.; Li, W.; Liu, S.; Yao, S.; Wang, C.; Shi, W.; daSilva, I.; Manuel, P.; Cheng, Y.; Daemen, L. D.; RamirezCuesta, A. J.; Tang, C.; Jiang, L.; Yang, S.; Guan, N.; Li, L. Control of Zeolite Pore Interior for Chemoselective Alkyne/Olefin Separations. *Science*. **2020**, *368*, 1002–1006.

[4] Liu, Y.; Wang, B.; Fu, Q.; Liu, W.; Wang, Y.; Gu, L.; Wang, D.; Li, Y. Polyoxometalate-Based Metal-Organic Framework as Molecular Sieve for Highly Selective Semi-Hydrogenation of Acetylene on Isolated Single Pd Atom Sites. *Angew. Chem. Int. Ed.* **2021**, *60*, 22522–22528.

[5] Shittu, T. D.; Ayodele, O. B. Catalysis of Semihydrogenation of Acetylene to Ethylene: Current Trends, Challenges, and Outlook. *Front. Chem. Sci. Eng.* **2022**, *16*, 1031–1059.

[6] Borodzinski, A.; Bond, G. C. Selective Hydrogenation of Ethyne in Ethene-Rich Streams on Palladium Catalysts, Part 2: Steady-State Kinetics and Effects of Palladium Particle Size, Carbon Monoxide, and Promoters. *Catal. Rev*. **2008**, *50*, 379-469.

[7] Ball, M. R.; Rivera-Dones, K. R.; Gilcher, E. B.; Ausman, S. F.; Hullfish, C. W.; Leborón, E. A.; Dumesic, J. A. AgPd and CuPd Catalysts for Selective Hydrogenation of Acetylene. *ACS Catal*. **2020**, *10*, 8567−8581.

[8] Maryam, T. R.; Saeed, S.; Samane, K. Acetylene Selective Hydrogenation: A Technical Review on Catalytic Aspects. *Rev. Chem. Eng*. **2018**, *34*, 215−237.

[9] Jian, M.; Liu, J.; Li, W. Hydroxyl Improving the Activity, Selectivity and Stability of Supported Ni Single Atoms for Selective Semi-Hydrogenation. *Chem. Sci.* **2021**, *12*, 10290-10298.

[10] Li, Z.; Zhang, J.; Tian, J.; Fang, K.; Jiang, Z.; Yan, B. Unveiling the Origin of Enhanced Catalytic Performance of NiCu Alloy for Semi-Hydrogenation of Acetylene. *Chem. Eng. J*. **2022**, 138244.

[11] Kruppe, C. M.; Krooswyk, J. D.; Trenary, M. Selective Hydrogenation of Acetylene to Ethylene in the Presence of a Carbonaceous Surface Layer on a Pd/Cu(111) Single-Atom Alloy. *ACS Catal.* **2017**, *7*, 8042-8049.

[12] Zhang, L.; Chen, Z.; Liu, Z.; Bu, J.; Ma, W.; Yan, C.; Bai, R.; Lin, J.; Zhang, Q.; Liu, J.; Wang, T.; Zhang, J. Efficient Electrocatalytic Acetylene Semihydrogenation by Electron–Rich Metal Sites in N–Heterocyclic Carbene Metal Complexes. *Nat. Commun.* **2021**, *12*, 6574.

[13] Azizi, Y.; Petit, C.; Pitchon, V. Formation of Polymer-Grade Ethylene by Selective Hydrogenation of Acetylene over Au/CeO_2 Catalyst. *J. Catal.* **2008**, *256*, 338-344.

[14] Cao, Y.; Zhang, H.; Ji, S.; Sui, Z.; Jiang, Z.; Wang, D.; Zaera, F.; Zhou, X.; Li, Y. Adsorption Site Regulation to Guide Atomic Design of Ni-Ga Catalysts for Acetylene Semi-Hydrogenation. *Angew. Chem. Int. Ed.* **2020**, *59*, 11647−11652.

[15] Liu, Y.; Liu, X.; Fang, Q.; He, D.; Zhang, L.; Lian, C.; Shen, R.; Zhao, G.; Ji, Y.; Wang, D.; Zhou, G.; Li, Y. Intermetallic Ni_xM_y (M = Ga and Sn) Nanocrystals: A Non-precious Metal Catalyst for Semi-Hydrogenation of Alkynes. *Adv. Mater*. **2016**, *28*, 4747−4754.

[16] Ferrando, R.; Jellinek, J.; Johnston, R. L. Nanoalloys: From Theory to Applications of Alloy Clusters and Nanoparticles. *Chem. Rev.* **2008**, *108*, 846−904.

[17] Zhao, S.; Osetsky, Y.; Zhang, Y. Diffusion of Point Defects in Ordered and Disordered Ni-Fe Alloys. *J. Alloys Compd.* 2019, *805*, 1175-1183.

[18] Escudero-Escribano, M.; Malacrida, P.; Hansen, M. H.; Vej-Hansen, U. G.; Velázquez-Palenzuela, V.; Tripkovic, J.; Schiøtz, J.; Rassmeisl, I. E. L.; Stephens, I.; Chorkendorff, A. Tuning the Activity of Pt Alloy Electrocatalysts by Means of the Lanthanide Contraction. *Science* **2016**, *352*, 73–76.

[19] Yang, C.; Wang, L.; Yin, P.; Liu, J.; Chen, M.; Yan, Q.; Wang, Z.; Xu, S.; Chu, S.; Cui, C.; Ju, H.; Zhu, J.; Lin, Y.; Shui, J.; Liang, H. Sulfur-Anchoring Synthesis of Platinum Intermetallic Nanoparticle Catalysts for Fuel Cells. *Science* **2021**, *374*, 459–464.

[20] Wang, D.; Xin, H.; Hovden, R.; Wang, H.; Yu, Y.; Muller, D. A.; DiSalvo, F. J. Abruña, H. D. Structurally Ordered Intermetallic Platinum-Cobalt Core-Shell Nanoparticles with Enhanced Activity and Stability as Oxygen Reduction Electrocatalysts. *Nat. Mater.* **2013**, *12*, 81–87.

[21] Chriatiansen, M. A.; Mpourmparkis, G.; Vlachos, D. G. Density Functional Theory-Computed Mechanisms of Ethylene and Diethyl Ether Formation from Ethanol on γ-Al_2O_3(100). *ACS Catal.* **2013**, *3*, 1965−1975.

[22] Divins, N. J.; Angurell, I.; Escudero, C.; Perez-Dieste, V.; Llorca, J. Influence of the Support on Surface Rearrangements of Bimetallic Nanoparticles in Real Catalysts. *Science* **2014**, *346*, 620−623.

[23] Yang, L.; Shan, S.; Loukrakpam, R.; Petkov, V.; Ren, Y.; Wanjala, B. N.; Engelhard, M. H.; Luo, J.; Yin, J.; Chen, Y.; Zhong, C. Role of Support-Nanoalloy Interactions in the Atomic-Scale Structural and Chemical Ordering for Tuning Catalytic Sites. *J. Am. Chem. Soc.* **2012**, *134*, 15048−15060.

[24] Liu, Y.; McCue, A. J.; Yang, P.; He, Y.; Zheng, L.; Cao, X.; Man, Y.; Feng, J.; Anderson, J. A.; Li, D. Support Morphology-Dependent Alloying Behaviour and Interfacial Effects of Bimetallic Ni-Cu/CeO_2 Catalysts. *Chem. Sci.* **2019**, *10*, 3556−3566.

[25] Dixit, M.; Kostetskyy, P.; Mpourmpakis, G. Structure-Activity Relationships in Alkane Dehydrogenation on γ-Al_2O_3: Site-Dependent Reactions. *ACS Catal*. **2018**, *8*, 11570−11578.

[26] Kwak, J.; Hu, J.; Mei, D.; Yi, C.; Kim, D.; Peden, C.; Allard, L.; Szanyi, J. Coordinatively Unsaturated Al^{3+} Centers as Binding Sites for Active Catalyst Phases of Platinum on γ-Al_2O_3. *Science*. **2009**, *325*, 1670–1673.

[27] (a) Ji, H.; Miao, S.; Ma, B.; Shen, Z.; Ling, F.; Wang, S.; Xiao, J.; Fu, R. Study on Relationship Between Surface Properties and Crystal Characteristics of γ-Al_2O_3. *Speciality Petrochemicals*, **2014**, *31*, 38-43; (b) Guo, Q.; Shen, Z.; Ling, F.; Yang, W.; Guo, C.; Ji, H.; Hu, Q. Synthesis and Characterization of Nanosized γ-Al_2O_3 with High Index Surface Planes. *Contemporary Chemical Industry*, **2015**, *44*, 951-954.

[28] Shi, L.; Deng, G.; Li, W.; Miao, S.; Wang, Q.; Zhang, W.; Lu, A. Al_2O_3 Nanosheets Rich in Pentacoordinate Al^{3+} Ions Stabilize Pt-Sn Clusters for Propane Dehydrogenation. *Angew. Chem. Int. Ed*. **2015**, *54*, 13994-13998.

[29] Hoch, M.; Johnston, H. L. Formation, Stability and Crystal Structure of the Solid Aluminium Suboxides: Al_2O and AlO. *J. Am. Chem. Soc.* **1954**, *76*, 2560-2561.

[30] Digne, M.; Sautet, P.; Raybaud, P.; Euzen, P.; Toulhoat, H. Use of DFT to Achieve a Rational Understanding of Acid-Basic Properties of γ-alumina Surfaces. *J. Catal*. **2004**, *226*, 54–68.

[31] Huang, H.; Shen, K.; Chen, F.; Li, Y. Metal−Organic Frameworks as a Good Platform for the Fabrication of Single-Atom Catalysts, *ACS Catal.* **2020**, *10*, 6579−6586.

[32] Shu, S.; Guo, J.; Liu, X.; Wang, X.; Yin, H.; Luo, D. Effects of Pore Sizes and Oxygen-Containing Functional Groups on Desulfurization Activity of Fe/NAC Prepared by Ultrasonic-Assisted Impregnation. *Appl. Surf. Sci.* **2016**, *360*, 684-692.

[33] Przepiorski, J. Deposition of Additives onto Surface of Carbon Materials by Blending Method—General Conception. *Materials Chemistry and Physics.* **2005**, *92*, 1-4.

[34] Zhao, G.; Hu, D.; Zhou, S.; Zhang, J.; Wang, L. Supported CuNi Alloy Catalyzed N-Alkylation of Bioderived 2,5-Dihydroxymethylfuran with Aniline. I*nd. Eng. Chem. Res.* **2019**, *58*, 6309−6315.

[35] Shan, J.; Janvelyan, N.; Li, H.; Liua, J.; Eglec, T. M.; Yec, J.; Biener, M. M.; Biener, J.; Friend, C. M.; Flytzani-Stephanopoulos, M. Selective Non-Oxidative Dehydrogenation of Ethanol to Acetaldehyde and Hydrogen on Highly Dilute NiCu Alloys. *Appl. Catal. B Environ.* **2017**, *205*, 541-550.

[36] Moya, S. F.; Martins, R. L.; Schmal, M. Monodispersed and Nanostructrured Ni/SiO_2 Catalyst and Its Activity for Non Oxidative Methane Activation. *Appl. Catal. A: Gen.* **2011**, *396*, 159-169.

[37] Richard, A. R.; Fan, M. Low-Pressure Hydrogenation of CO_2 to CH_3OH Using Ni-In-Al/SiO_2 Catalyst Synthesized Via a Phyllosilicate Precursor. *ACS Catal*. **2017**, *7*, 5679−5692.

[38] Zhu, X.; Zhang, Y.; Liu, C. CO Adsorbed Infrared Spectroscopy Study of Ni/Al_2O_3 Catalyst for CO_2 Reforming of Methane. *Catal. Lett.* 2007, *118*, 306–312.

[39] Li, C.; Chen, Y.; Zhang, S.; Zhou, J.; Wang, F.; He, S.; Wei, M.; Evans, D. G.; Duan, X. Nickel-Gallium Intermetallic Nanocrystal Catalysts in the Semi-Hydrogenation of Phenylacetylene. *ChemCatChem* **2014**, *6*, 824-831.

[40] Fu, B.; McCue, J. A.; Liu, Y.; Weng, S.; Song, Y.; He, Y.; Feng, J.; Li, D. Highly Selective and Stable Isolated Non-Noble Metal Atom Catalysts for Selective Hydrogenation of Acetylene. A*CS Catal*. **2022**, *12*, 607-617.

[41] Osswald, J.; Giedigkeit, R.; Jentoft, R. E.; Armbrüster, M.; Girgsdies, F.; Kovnir, K.; Ressler, T.; Grin, Y.; Schlçgl, R. Palladium–Gallium Intermetallic Compounds for the Selective Hydrogenation of Acetylene: Part I: Preparation and Structural Investigation under Reaction Conditions. *J. Catal.* **2008**, *258*, 210-218.

[42] Wang, Y.; Furukawa, S.; Yan, N. Identification of an Active NiCu Catalyst for Nitrile Synthesis from Alcohol. *ACS Catal.* **2019**, *9*, 6681-6691.

[43] Malta, G.; Kondrat, S. A.; Freakley, S. J.; Davies, C. J.; Dawson, S.; Liu, X.; Lu, L.; Dymkowski, K.; Fernandez-Alonso, F.; Mukhopadhyay, S.; Gibson, E. K.; Wells, P. P.; Parker, S. F.; Kiely, C. J.; Hutchings, G. J. Deactivation of a Single-Site Gold-on-Carbon Acetylene Hydrochlorination Catalyst: An X-ray Absorption and Inelastic Neutron Scattering Study. *ACS Catal*. **2018**, *8*, 8493−8505.

[44] Sun, H.; Yang, J.; Zhang, H.; Yang, Q.; Wu, S.; Wang, Y.; Zhu, H.; Yue, Y.; Wang, T.; Yuan, P. Hierarchical Flower-Like NiCu/SiO_2 Bimetallic Catalysts with Enhanced

Catalytic Activity and Stability for Petroleum Resin Hydrogenation. *Ind. Eng. Chem. Res.* 2021, *60*, 5432-5442.

[45] Miao, C.; Zhou, G.; Chen, S.; Xie, H.; Zhang, X. Synergistic Effects Between Cu and Ni Species in NiCu/γ-Al_2O_3 Catalysts for Hydrodeoxygenation of Methyl Laurate. *Renewable Energy* **2020**, *153*, 1439−1454.

[46] Hussain Motagamwala, A.; Almallahi, R.; Wortman, J.; Omoze Igenegbai, V.; Linic, S. Stable and Selective Catalysts for Propane Dehydrogenation Operating at Thermodynamic Limit. *Science* **2021**, *373*, 217–222.

[47] Ma, H.; Wang, G. Selective Hydrogenation of Acetylene on Pt_n/TiO_2 (n = 1, 2, 4, 8) Surfaces: Structure Sensitivity Analysis, *ACS Catal.* **2020**, *10* (9), 4922-4928.

[48] Wang, Y.; Liu, B.; Lan, X.; Wang, T. Subsurface Carbon as a Selectivity Promotor to Enhance Catalytic Performance in Acetylene Semi-Hydrogenation. *ACS Catal.* **2021**, *11*, 10257−10266.

[49] Zhang, H.; Liu, Y.; Chao, T.; Zhang, J.; Zhang, J.; Lou, X. Unveiling the Activity Origin of Electrocatalytic Oxygen Evolution over Isolated Ni Atoms Supported on a N-Doped Carbon Matrix. *Adv Mater*. **2019**, *31*, 1904548.

[50] Chu, M.; Pan, Q.; Bian, W.; Liu, Y.; Cao, M.; Zhang, C.; Lin, H.; Zhang, Q.; Xu, Y. Strong Metal-Support Interaction Between Palladium and Gallium Oxide within Monodisperse Nanoparticles: Self-Supported Catalysts for Propyne Semi-Hydrogenation. *J. Catal*. **2021**, *395*, 36−45.

[51] Jackson, S. D.; Casey, N. J. Hydrogenation of Propyne over Palladium Catalysts. *J. Chem. Soc. Faraday Trans*. **1995**, *91*, 3269−3274.

[52] Abdel-Rahman, M. K.; Trenary, M. Propyne Hydrogenation over A Pd/Cu (111) Single-Atom Alloy Studied using Ambient Pressure Infrared Spectroscopy. *ACS Catal*. **2020**, *10*, 9716−9724.

[53] Ge, X.; Dou, M.; Cao, Y.; Liu, X.; Qi, Y.; Zhang, J.; Qian, G.; Gong, X.; Zhou, X.; Chen, L.; Yuan, W.; Duan, X. Mechanism Driven Design of Trimer Ni_1Sb_2 Site Delivering Superior Hydrogenation Selectivity to Ethylene. *Nat. Commun.* **2022**, *13*, 5534.

[54] Cao, Y.; Ge, X.; Li, Y.; Si, R.; Sui, Z.; Zhou, J.; Duan, X.; Zhou, X. Corrigendum to “Structural and Kinetics Understanding of Support Effects in Pd-Catalyzed Semi-

Hydrogenation of Acetylene". *Engineering PRC*. **2021**, *7*, 103−110.

[55] Li, R.; Yue, Y.; Chen, Z.; Chen, X.; Wang, S.; Jiang, Z.; Wang, B.; Xu, Q.; Han, D.; Zhao, J. Selective Hydrogenation of Acetylene over Pd-Sn Catalyst: Identification of Pd_2Sn Intermetallic Alloy and Crystal Plane-Dependent Performance. *Appl. Catal. B*, **2020**, *279*, 119348.

[56] Zhou, H.; Yang, X.; Li, L.; Liu, X.; Huang, Y.; Pan, X.; Wang, A.; Li, J.; Zhang, T. PdZn Intermetallic Nanostructure with Pd-Zn-Pd Ensembles for Highly Active and Chemoselective Semi-Hydrogenation of Acetylene. *ACS Catal*. **2016**, *6*, 1054−1061.

[57] Rao, D.; Zhang, S.; Li, C.; Chen, Y.; Pu, M.; Yan, H.; Wei, M. The Reaction Mechanism and Selectivity of Acetylene Hydrogenation over Ni-Ga Intermetallic Compound Catalysts: A Density Functional Theory Study. *Dalton Trans*, **2018**, *47*, 4198−4208.

Graphical abstract

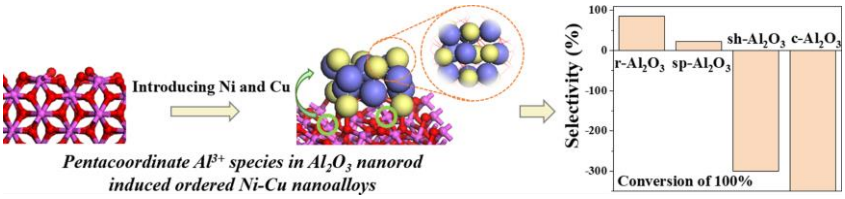

Supporting information

Understanding the Role of Coordinatively Unsaturated Al^{3+} Sites on Nanoshaped Al_2O_3 for Creating Uniform Ni-Cu Alloys for Selective Hydrogenation of Acetylene

Yuanfei Song, [1] Shaoxia Weng, [1] Fan Xue,[2] Alan J. McCue,[3,*] Lirong Zheng[4], Yufei He, [1] Junting Feng, [1] Yanan Liu,[1,*] Dianqing Li[1,*]

[1]*State Key Laboratory of Chemical Resource Engineering, Beijing Engineering Center for Hierarchical Catalysts, Beijing University of Chemical Technology, Beijing, 100029, China*

[2] *Institute of Solid State Chemistry, University of Science and Technology Beijing, Beijing 100083, People's Republic of China*

[3] *Department of Chemistry, University of Aberdeen, Aberdeen AB24 3UE, U.K.*

[4] *High Energy Physics, Chinese Academy of Sciences, Beijing 100049, China*

* Corresponding author

Address: Box 98, 15 Bei San Huan East Road, Beijing 100029, China

Tel: +86 10 64436992 Fax: +86 10 64436992

E-mail address: a.mccue@abdn.ac.uk (Alan J. McCue); ynliu@mail.buct.edu.cn (Yanan Liu); lidq@mail.buct.edu.cn (Dianqing Li)

1. EXPERIMENTAL DETAIL

1.1 Materials. $Ni(NO_3)_2{\cdot}6H_2O$, $Cu(NO_3)_2{\cdot}3H_2O$, $NaAlO_2$, NH_4HCO_3, $AlCl_3{\cdot}6H_2O$, $Al(NO_3)_3{\cdot}9H_2O$ and NaOH were purchased in AR grade. The pseudo boehmite was obtained by from the Liming Research Institute of Chemical Industry. A conventional γ-alumina was purchased from Macklin.

1.2 Preparation of nanoshaped Al_2O_3 samples. A series of nanoshaped aluminas were synthesized as described below[1]. Firstly, alumina nanorods were prepared. Pseudo-boehmite was calcined in a muffle furnace at 600 ℃ for 4 h to form 10 g of alumina powder which was then mixed with 15 g of NH_4HCO_3 in 400 mL of deionized water. After stirring for 20 min, the mixture was transferred into a teflon-lined stainless steel autoclave, followed by heating to 140 ℃ for 6 h. After cooling to room

temperature, the white solid precipitate was collected by use of a centrifuge, washed until neutrality and then dried at 120 ℃. Lastly, the obtained powder was calcined at 600 ℃ with a heating rate of 10 ℃·min^{-1} for 4 h to obtain the alumina nanorods (denoted as r-Al_2O_3 throughout).

Alumina with a sheet or platelet type morphology was prepared as follows[2]. $NaAlO_2$ and $Al(NO_3)_3$ solutions with a concentration of 2 mol L^{-1} were prepared. The former was added dropwise into 200 mL of $Al(NO_3)_3$ solution under magnetic stirring until pH of the solution reached to ~9.5. After stirring for 1 h at 140 ℃, the mixture was transferred into a Teflon-lined stainless autoclave, followed by heating to 200℃ for 24 h. After cooling to room temperature, the precipitate was collected, washed, dried and calcined as described for the r-Al_2O_3 sample. In this case the final product is denoted as sh-Al_2O_3.

Alumina with a spindle like morphology (i.e., a rod that is not perfectly cylindrical in shape but has a convex shape along the longest dimension that equates to a gradual curvature of the surface) was prepared as follows[3]. $AlCl_3·6H_2O$ and NaOH solutions with a concentration of 2 mol/L were prepared. NaOH solution was added dropwise to the $AlCl_3$ solution under magnetic stirring until the OH^-/Al^{3+} molar ratio reached 3. The solution was then stirred for 15 min to allow aluminum hydroxide to form. The precipitate was collected and transferred into a Teflon-lined stainless autoclave to be heated to 200℃ for 24 h. After this thermal treatment the sample is denoted as sp-Al_2O_3.

1.3 Preparation of Ni-Cu/Al_2O_3 catalysts. The nanoshaped Al_2O_3 samples were then used as support to prepare a series of bimetallic Ni-Cu catalysts by using a wetness impregnation method. Typically, 0.1900 g $Cu(NO_3)_2·3H_2O$ and 0.2900 g $Ni(NO_3)_2·6H_2O$ was dissolved in 10 mL of deionized water (these amounts equate to 5 wt. % loading of Ni and Cu, respectively). Then, 1.0000 g of a particular nanoshaped Al_2O_3 was added into the above solution. After stirring vigorously for 4 h, the resulting paste was dried at 60 °C overnight before being calcined at 500 °C for 4 h and subsequently reduced in 10% H_2/N_2 at 500 °C for 4 h (heating rate of 10 °C min^{-1}). The as-prepared catalysts were denoted as Ni-Cu/r-Al_2O_3, Ni-Cu/sh-Al_2O_3 and Ni-Cu/sp-Al_2O_3. For comparison, a commercial Al_2O_3 supported Ni-Cu catalyst was prepared

using the same impregnation procedure described above and this sample is denoted as Ni-Cu/c-Al_2O_3.

1.4 Catalyst characterization. A Shimadzu XRD-6000 diffractometer with Cu Kα radiation (λ = 0.154 nm) was used to collect X-ray Diffraction (XRD) patterns in the 2θ range 10-90° with a scan speed of 10° min^{-1}. A Shimadzu ICPS-7500 Inductively Coupled Plasma Atomic Emission Spectrometer (ICP-AES) was used to quantify the metal loadings of catalyst samples. The specific surface areas were calculated from N_2 adsorption data and the relative pressure range 0.05-0.3 using the Brunauer-Emmett-Teller (BET) method. Cs-corrected STEM images were measured on a JEOL ARM200F microscope equipped with a spherical aberration corrector and a High-Angle Annular Dark-Field detector (HAADF), which allows for Z contrast imaging. A Thermo ESCALAB 250Xi X-ray Photoelectron Spectrometer (XPS) with monochromatic Al K_a (hv =1486.6 eV) was used to analyze the surface/near surface composition and electronic structure. The sample was placed in the pool and in situ reduced in 10% H_2/Ar at 500ºC for 30 min to avoid re-oxidation in air. Cu 2p and Ni 2p regions were analyzed using CasaXPS software with the C 1s peak at 284.8 eV used for calibration. Solid State NMR spectra were recorded on Bruker 400WB AVANCE III instrument. ^{27}Al NMR experiments were carried out using a 4 mm triple-resonance broadband solid-state probe with a spinning rate of 8 kHz. The spectra were accumulated for 120 scans with 2 s recycle delay. The chemical shifts were referenced to a 1% $Al(NO_3)_3$ aqueous solution. Thermo Gravimetric Analysis (TGA) profiles were recorded using a HITACHI STA7300 instrument. The samples were heated in the temperature range 30-800 ℃ with a rate of 10 ℃ min^{-1} under a flow of air. The evolved gases from TGA experiments were analyzed by mass spectrometry (m/z = 44 used to follow CO_2 loss from the sample). Temperature programmed experiments were performed using a Micrometrics ChemiSorb 2750 instrument with a Thermal Conductivity Detector (TCD). Approximately 0.1 g of sample was placed in a quartz tube and pretreated to 200 ℃ for 0.5 h in Ar to remove surface impurities. For Temperature Programmed Reduction (TPR), samples were then heated from room temperature to 600 ℃ at a ramp rate of 10 ℃ min^{-1} in a flow of 10% H_2/Ar. For C_2H_4-

TPD experiments, the catalysts were first pre-reduced at 300 ℃ for 2 h in a 10 % H_2/Ar flow. After cooling to room temperature, the samples were exposed to a C_2H_4 flow for 1 h and then purged in He to remove any physically adsorbed species. For desorption, samples were then heated from 50-800 ℃ at a rate of 10 ℃/min. Fourier Transform Infrared spectra of adsorbed CO were obtained using a Bruker Tensor 27 instrument with a highly sensitive Mercury Cadmium Telluride (MCT) detector, a quartz reaction cell with BaF_2 windows using the diffuse reflectance mode. Sample powders were pre-reduced for 2 h in H_2/Ar at 300 ℃, followed by Ar purging for 0.5 h. After cooling the sample to 50 ℃ in Ar flow, a background spectrum was recorded (resolution of 4 cm^{-1}). Pure CO flow was introduced into the reactor for 0.5 h. Spectra of adsorbed CO then recorded after further purging with Ar for 1 h to remove any gas phase CO (it is expected that this treatment results in the loss of CO from Cu meaning the spectra predominantly represent CO adsorbed on Ni after Ar purging). In situ FTIR of alkyne hydrogenation using C_3H_4 as a representative reactant molecule were performed after the same pre-treatment and background spectrum process described above. For the reaction study, pure C_3H_4 was introduced for 0.5 h at room temperature, followed by Ar purging for 10 min to observe the characteristic peaks of adsorbed propyne. Then, H_2 was added with a flowing rate of 10 mL/min and the sample chamber heated stepwise to different temperatures (50, 70, 90 and 120 ℃) to observe reaction intermediates. X-ray Absorption find structure spectra (Ni K-edge and Cu K-edge) was conducted at the 1W1B beamline of the National Synchrotron Light Source II at the Beijing Synchrotron Radiation Facility. The sample was protected under N_2 atmosphere to prevent re-oxidation in air, followed by measurement in the transmission mode. The typical energy of the storage ring was 2.5 GeV with a maximum current of 250 mA. Using Si(111) double-crystal monochromator, the data collection were carried out in transmission/fluorescence mode using ionization chamber. The high energy X-ray scattering data was collected on the 3W1 beamline at Beijing Synchrotron Radiation Facility (BSRF) with the X-ray wavelength of 0.206468 Å. The Pair Distribution Function (PDF) analysis was obtained from high energy X-ray scattering data by direct

Fourier transform of reduced structure function by xPDF suite software and small box fitting was carried out based on PDF guide.

1.5 Computational method. Using the material studio software package, an initial structural model of gamma alumina was established with a slab size of 4.9 nm × 5.0 nm × 4.2 nm. Periodic boundary conditions were adopted in the X-Y direction and 5 nm vacuum layers were established on the upper and lower surfaces of alumina in the Z direction, corresponding to Al_2O_3 (100) and (111) facets, respectively. This was a convenient arrangement to observe the behavior of Ni and Cu atoms on the Al_2O_3 surface. Cvff force field was used to describe the interaction between Al, O, Cu and Ni atoms. The time step of the simulation process was set to 0.1 fs. After the structure was optimized using the conjugate gradient method, the external ambient temperature was set to 300 K, with NVT ensemble relaxation of 10 ps and the relaxation time for temperature control was 10 fs to make the substrate temperature reach the set temperature. Then, two Ni and Cu atoms were introduced on the surface of Al_2O_3 to observe the adsorption behavior of Ni and Cu atoms.

To explore the catalytic mechanism, first-principle spin-polarized calculation were conducted using Vienna ab initio Simulation Program (VASP)[4,5]. The generalized gradient approximation (GGA) in the Perdew-Burke-Ernzerhof (PBE) form and a cutoff energy of 500 eV for planewave basis set were employed[6]. A 3 × 3 × 1 Monkhorst-Pack k grid was adopted for sampling Brillouin zones at structure calculation[7]. The Projector Augmented Wave (PAW) method was used to describe ion-electron interactions[8]. The 1 × 3 Al_2O_3 (100) slab (a =14.277 Å, b = 12.991 Å) was modeled with a vacuum space exceeding 20 Å to avoid interaction between two periodic units. The convergence criteria for structure optimization were selected as the maximum force on each atom being less than 0.02 eV/Å with an energy change of less than 1×10^{-5} eV. The van der Waals interactions in these systems was described by Grimme's DFT-D3 scheme of dispersion correction[9]. To calculate the kinetic energy barrier of chemical reactions, the Climbing Image Nudged Elastic Band (CI-NEB) method was employed to search for the transition states[10,11].

The Gibbs free energy change (ΔG) for each elemental step is defined as[12,13]:

$$\Delta G = \Delta E + \Delta ZPE - T\Delta S \cdot$$

where ΔE and ΔZPE are the adsorption energy based on density functional theory calculations and the zero-point energy correction, respectively. T and ΔS represent the temperature and the entropy change, respectively.

1.6 Catalytic testing. Catalytic behavior was evaluated in a fixed-bed microreactor operating at a pressure of 0.1 MPa and temperature in the range 30-130℃. For tests, 0.3 g of catalyst was diluted with quartz sand (Aldrich, 40-70 mesh) and placed in the reactor. The inlet gas feed consisted of a 0.31% C_2H_2/30.4% C_2H_4/1.0 % C_3H_8/3.1% H_2 mixture diluted by nitrogen with flow rate that equated to a Gas Hourly Space Velocity (GHSV) of 9680 h^{-1}. The reactant and product concentrations were analyzed by online Gas Chromatography (GC) with a flame ionization detector using a PLOT capillary column (50 m × 0.53 mm). Propane was used as an internal standard. Multiple data points were collected at different temperatures to ensure reproducibility. Acetylene conversion is defined as the ratio of the reactant consumed to the reactant feed. The selectivity to ethylene was calculated as the amount produced divided by the amount of acetylene consumed. By this metric a negative ethylene selectivity is possible and implies a portion of the ethylene presented in the feed gas was also hydrogenated. The selectivity to oligomers was calculated based on carbon balance (100 ± 0.5%). The specific activity was calculated according to the total Ni content. TOF (s^{-1}) was calculated according to the amount of exposed surface Ni atoms. The equations used were as follows:

$$\text{Acetylene conversion (\%)} = \frac{C_2H_2(\text{inlet}) - C_2H_2(\text{outlet})}{C_2H_2(\text{inlet})}$$

$$\text{Ethylene selectivity (\%)} = \frac{C_2H_4(\text{outlet}) - C_2H_4(\text{inlet})}{C_2H_2(\text{inlet}) - C_2H_2(\text{outlet})}$$

$$\text{TOF} = \frac{C \times L \times M \times 10^{-3}}{V_m \times m \times w \times D \times 60}$$

where C_2H_2 (inlet), C_2H_4 (inlet), C_2H_2 (outlet) and C_2H_4 (outlet) represent reactant/product concentrations, C is conversion of acetylene (%); L is the flow rate of

acetylene (mL min^{-1}); V_m is molar volume of gas (L mol^{-1}); M stands for atomic mass of Ni; m is quality of catalyst (g); w is the metal loading (wt. %); D is metal dispersion (%). The apparent activation energies were determined but using a reaction temperature where acetylene conversion was below 15%. To test for catalyst stability, additional tests were performed for a continuous 12 h period at a constant temperature of 115ºC.

2. ADDITIONAL RESULTS

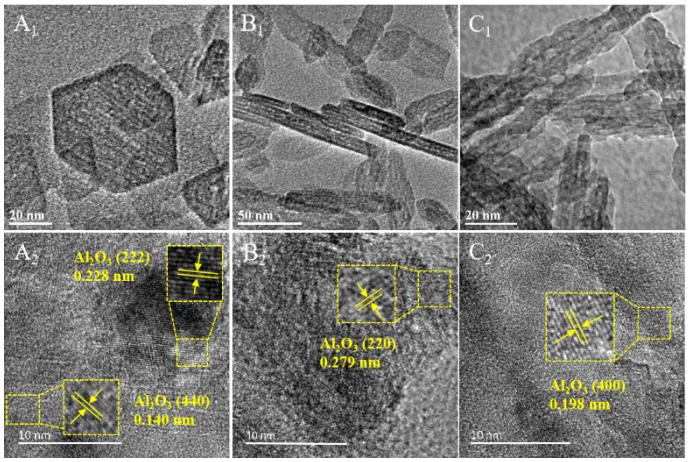

Figure S1 HRTEM images of (A) sh-Al_2O_3, (B) sp-Al_2O_3, (C) r-Al_2O_3

Table S1 The proportion of different coordinated Al species before and after metal loading

Coordinated Al species	Al_{VI} (%)	Al_V (%)	Al_{IV} (%)
sh-Al_2O_3	71.5	4.3	24.2
sp-Al_2O_3	64.2	7.5	28.3
r-Al_2O_3	55.7	15.8	28.5
Ni-Cu/sh-Al_2O_3	75.1	3.6	21.3
Ni-Cu/sp-Al_2O_3	69.9	6.0	24.1
Ni-Cu/r-Al_2O_3	62.6	9.7	27.7

Table S2 Properties of Ni-Cu/Al_2O_3 catalysts

	NiCu/sh-Al_2O_3	NiCu/sp-Al_2O_3	NiCu/r-Al_2O_3	NiCu/c-Al_2O_3
d_{VA} (nm) [a]	7.5	11.3	5.6	-
Ni loading (wt. %) [b]	4.6	4.7	4.7	4.4
Cu loading (wt. %) [b]	4.5	4.6	5.0	4.5
D (%) [c]	13.5	8.9	18.0	-
E_a (kJ/mol)	34.8	35.6	38.4	73.2

[a] Determined by HRTEM analysis; [b] Determined by ICP result;

[c] Based on HRTEM analysis[11], $D = \frac{V_M/A_M}{d_{VA}}$; V_M (the volume of metal atom) = 10.95 Å^3; A_M (surface area of metal atom) = 6.51 Å^2

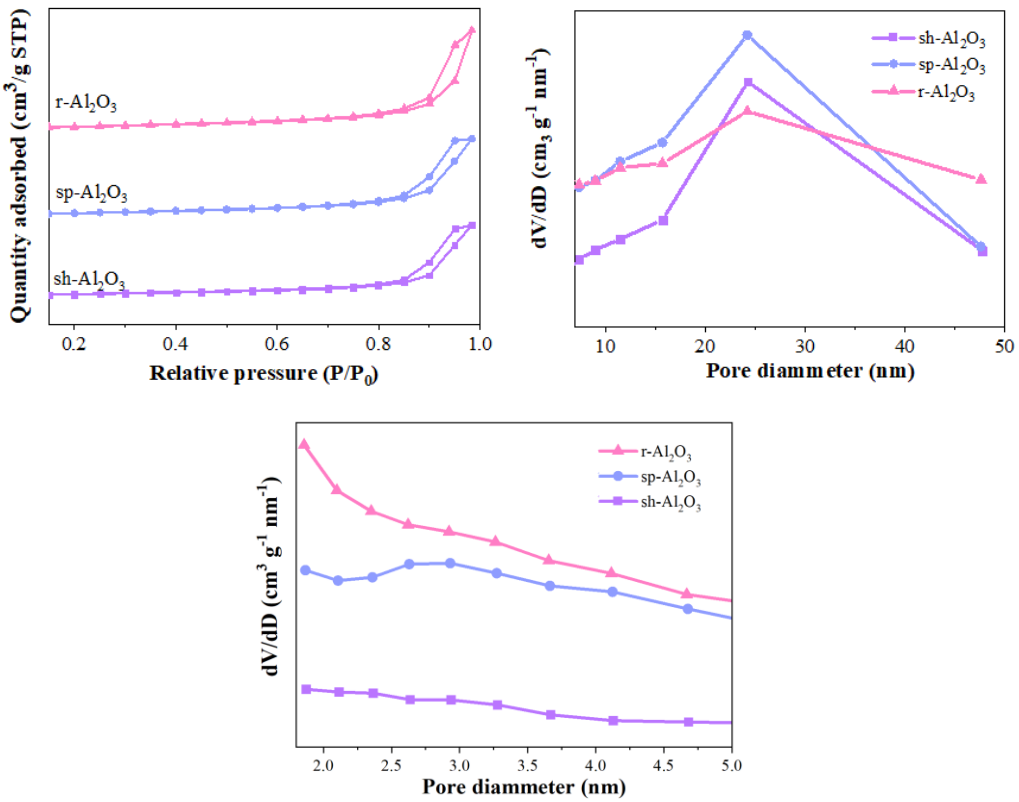

Figure S2 N_2 adsorption-desorption isotherms and pore size distribution curves for the prepared sh-Al_2O_3, sp-Al_2O_3 and r-Al_2O_3

Table S3 Surface area, pore volume and size of nanoshaped Al_2O_3

Catalysts	Surface area (m^2/g)	Pore volume (cm^2/g)	Pore diameter (nm)
sh-Al_2O_3	84	0.50	20.40
sp-Al_2O_3	112	0.50	18.70
r-Al_2O_3	186	1.50	31.70

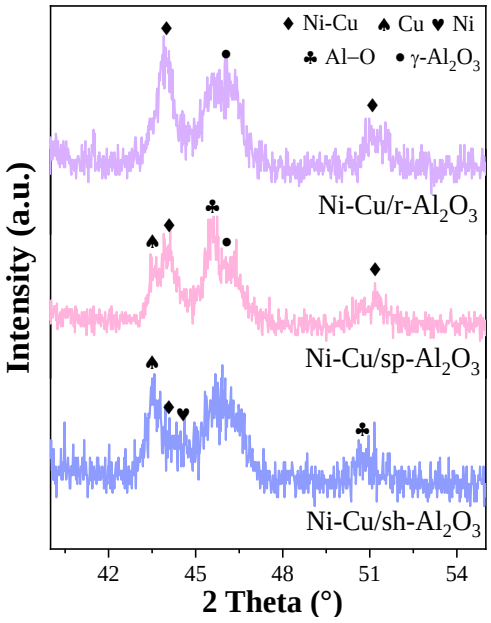

Figure S3 XRD patterns of Ni-Cu/sh-Al_2O_3, Ni-Cu/sp-Al_2O_3 and Ni-Cu/r-Al_2O_3

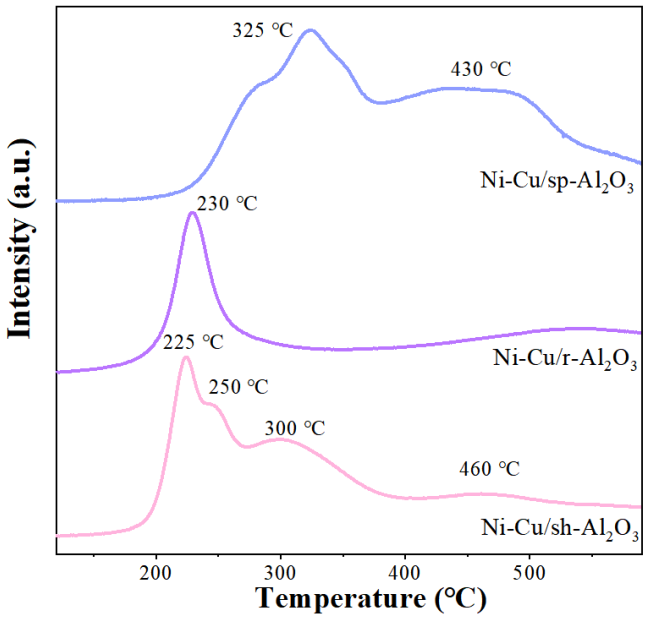

Figure S4 TPR profiles for the prepared Ni-Cu catalysts

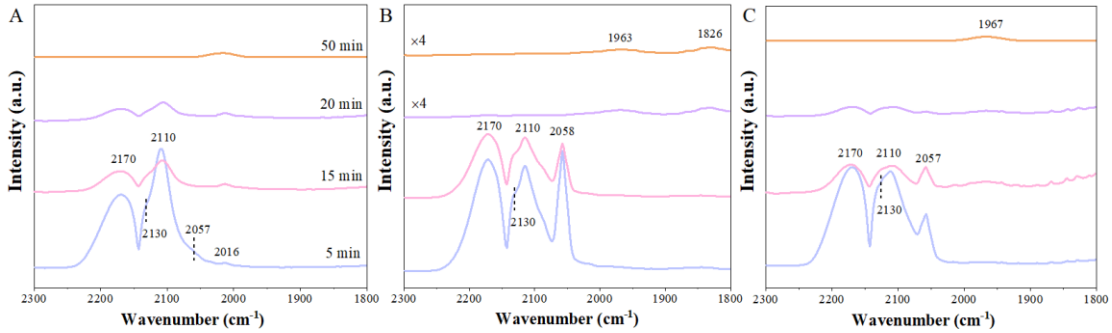

Figure S5 FTIR spectra of CO adsorption over (A) Ni-Cu/r-Al_2O_3 (B) Ni-Cu/sp-Al_2O_3 (C) Ni-Cu/sh-Al_2O_3

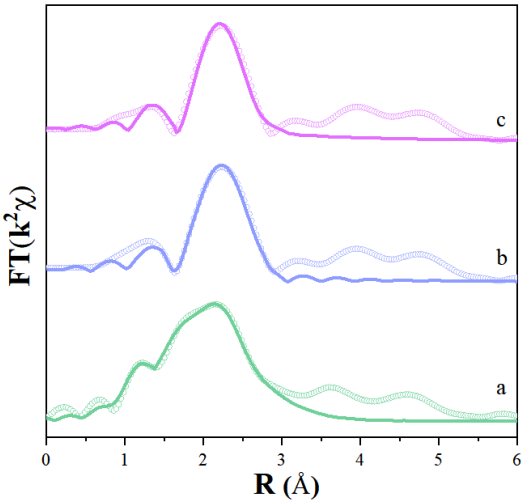

Figure S6 The fitted Fourier transform k^2-weighted Ni K-edge EXAFS spectra for (a) Ni-Cu/sh-Al_2O_3, (b) Ni-Cu/r-Al_2O_3 and (c) Ni-Cu/sp-Al_2O_3

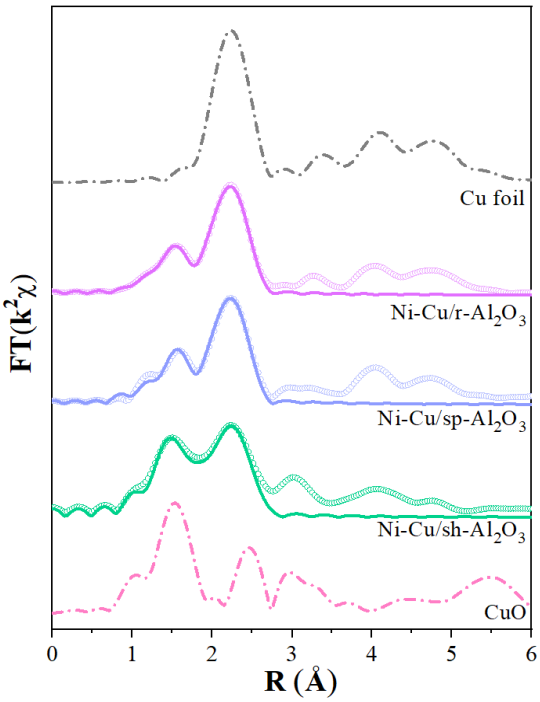

Figure S7 The fitted Fourier transform k^2-weighted Cu K-edge EXAFS spectra for Ni-Cu/sh-Al_2O_3, Ni-Cu/r-Al_2O_3 and Ni-Cu/sp-Al_2O_3 with CuO and Cu foil as the references

Table S4 Ni K-edge EXAFS parameters fitted for the samples

Samples	Scattering pair	CN[a]	r[b] (Å)	ΔE[c] (eV)	σ[2d]	R factor
Ni-Cu/r-Al_2O_3	Ni-Ni/Cu	5.9	2.51	-2.503	0.008	0.004
	Ni-O	2.3	2.06	-2.503	0.005	
Ni-Cu/sp-Al_2O_3	Ni-Ni/Cu	6.4	2.49	-2.156	0.008	0.005
	Ni-O	2.5	2.05	-2.156	0.007	
Ni-Cu/sh-Al_2O_3	Ni-Ni/Cu	6.0	2.48	-0.950	0.012	0.008
	Ni-O	2.8	2.07	-0.950	0.005	

[a] Coordination number (CN) [b] Atomic distance (r)

[c] Energy difference in the absorption threshold between the reference and the target samples (ΔE)

[d] Debye-Waller factor (σ^2)

Table S5 Cu K-edge EXAFS parameters fitted for the samples

Samples	Scattering pair	CN[a]	r[b] (Å)	ΔE[c] (eV)	σ[2d]	R factor
Ni-Cu/r-Al_2O_3	Cu-Cu/Ni	5.7	2.51	3.2	0.0105	0.005
	Cu-O	1.5	1.92	8.0	0.0072	
Ni-Cu/sp-Al_2O_3	Cu-Cu/Ni	6.5	2.53	4.8	0.0089	0.008
	Cu-O	2.2	1.94	8.1	0.0064	
Ni-Cu/sh-Al_2O_3	Cu-Cu/Ni	4.5	2.54	2.1	0.0111	0.009
	Cu-O	2.8	1.96	6.3	0.0122	

[a] Coordination number (CN) [b] Atomic distance (r)

[c] Energy difference in the absorption threshold between the reference and the target samples (ΔE)

[d] Debye-Waller factor (σ^2)

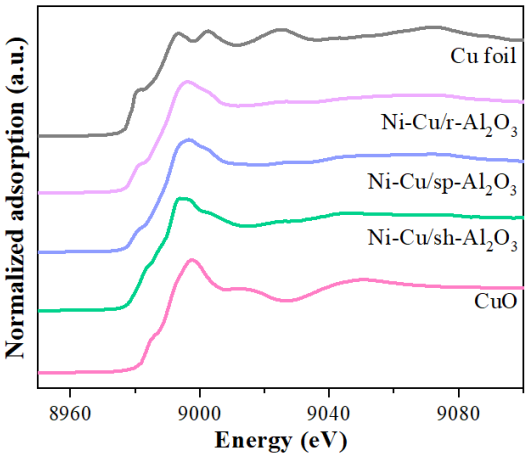

Figure S8 Normalized XANES spectra of Ni-Cu/Al_2O_3 catalysts with CuO and Cu foil as the references

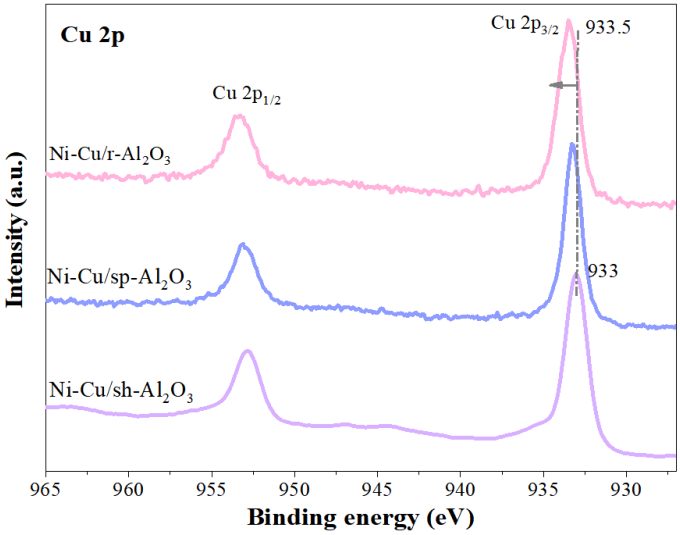

Figure S9 XPS spectra of Cu 2p for Ni-Cu catalysts

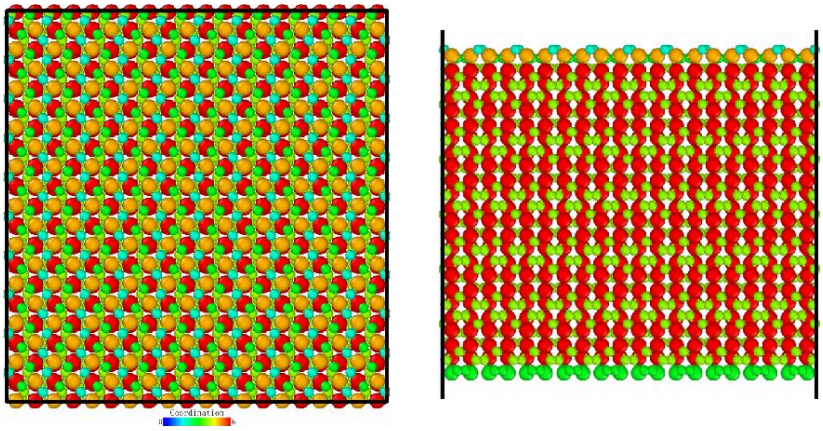

Figure S10 The structures model of Al_2O_3 with exposing (100) facet

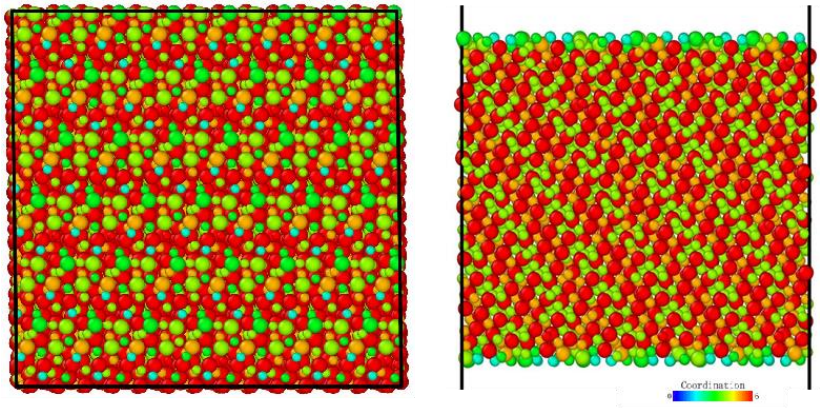

Figure S11 The structures model of Al_2O_3 with exposing (111) facet

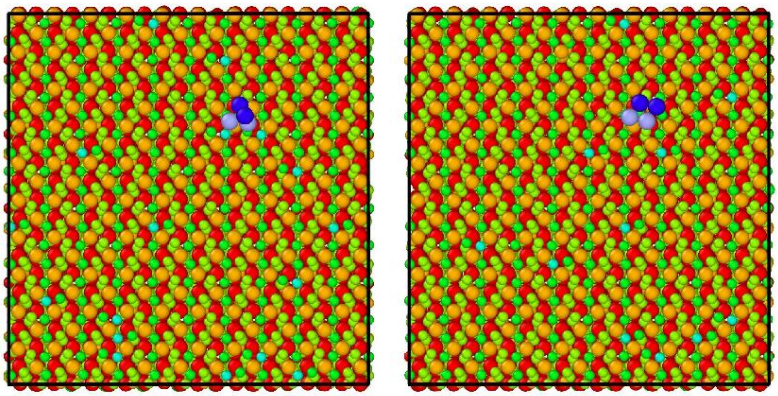

Figure S12 The possible position for the anchoring of Ni and Cu atoms on Al_2O_3 (100)

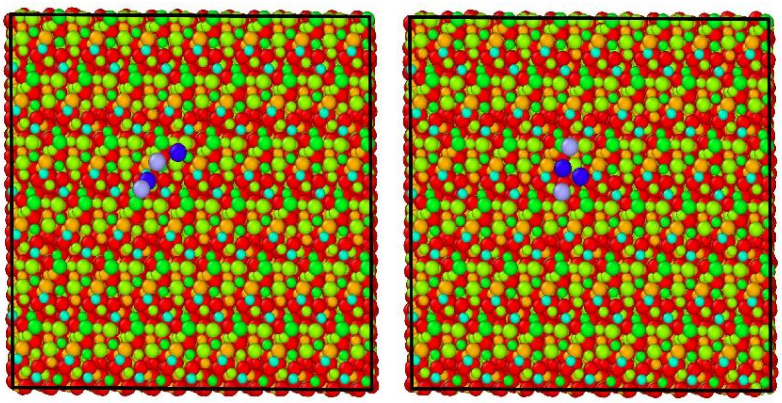

Figure S13 The possible position for the anchoring of Ni and Cu atoms on Al_2O_3 (111)

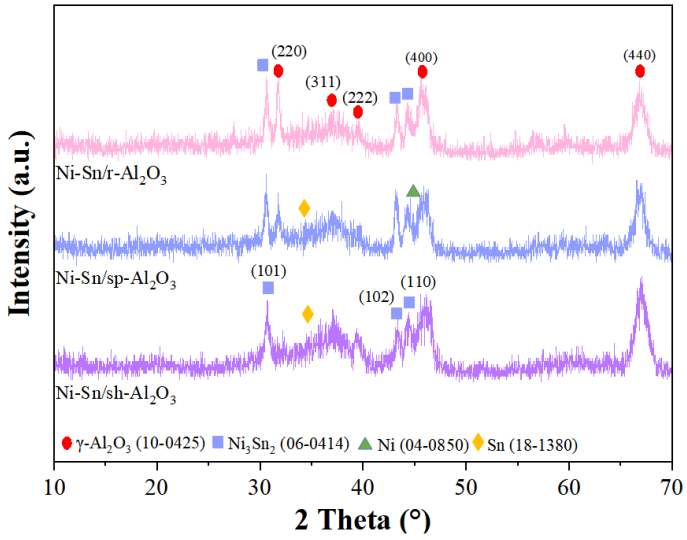

Figure S14 XRD patterns of nanoshaped Al_2O_3 supported Ni-Sn catalysts

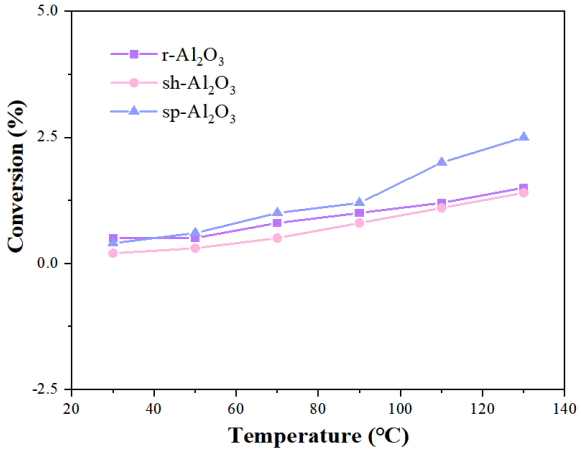

Figure S15 Acetylene conversion of nanoshaped Al_2O_3 supports

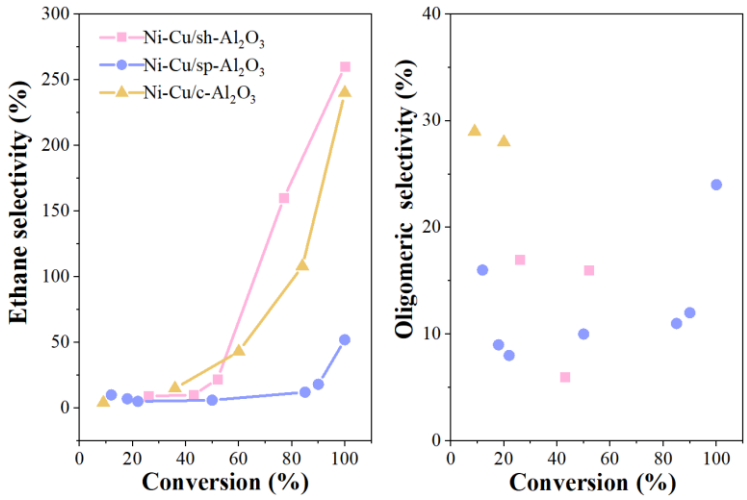

Figure S16 Ethane selectivity as a function of acetylene conversion of Ni-Cu/sh-Al_2O_3, Ni-Cu/sp-Al_2O_3 and Ni-Cu/c-Al_2O_3

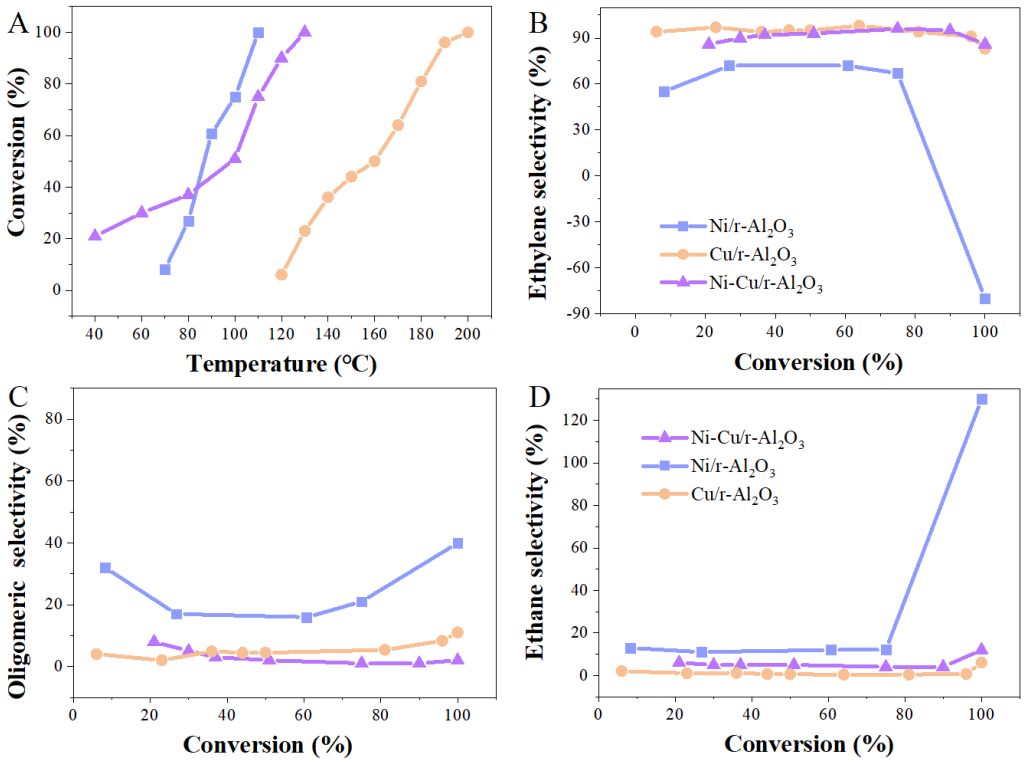

Figure S17 (A) Acetylene conversion as a function of temperature (B) ethylene selectivity, (C) oligomer selectivity (D) ethane selectivity as a function of conversion for r-Al_2O_3 supported bimetallic Ni-Cu, monometallic Ni and Cu samples (reaction conditions: 0.3 g of catalyst, 10:1 of H_2/C_2H_2 ratio, total flow = 163 mL min^{-1}, SV = 9780 h^{-1}, temperature in the range of 40-200 ^oC).

Table S6 Comparison of catalytic performance with Ni-based catalysts reported in literatures

Catalysts	H_2/ C_2H_2	SV (h^{-1})	T (℃)	Conv. (%)	Sel. (%)	Ea (kJ/mol)
Ni-Cu/r-Al_2O_3	10:1	9780	135	100	86	38.4
Ni_5Ga/SiO_2[14]	5:1	36000	180	100	81	-
$AuNi_1/SiO2$[15]	20:1	6000	300	100	80	-
$NiCu/SiO_2$[16]	4:1	30000	140	100	10	-
$AgNi/SiO_2$[17]	20:1	60000	200	100	31.4	-
NiS/Al_2O_3[18]	20:1	9900	160	100	78	-
Ni/Al_2O_3[18]	20:1	9900	220	100	-10	28.9
$NiZn/SiO_2$[19]	10:1	128000	200	15	80	27.5
Ni_6In/SiO_2[20]	5:1	36000	180	100	65	-
Ni/CeO_2[21]	4:1	21000	110	100	65	-
NiCu/MMO[22]	2:1	8040	160	100	70	34.2
NiGa/α-Al_2O_3[23]	4:1	4800	300	100	80	-
Ni_5Ga_3/α-Al_2O_3[23]	4:1	4800	300	100	60	-
Ni_3Ga/α-Al_2O_3[23]	4:1	4800	280	100	55	-
$CuNi_{0.125}/SiO_2$[24]	20:1	60000	300	100	60	54.5
$AgNi_{0.5}/SiO_2$[24]	20:1	60000	220	99	65	52.8
$AuNi_{0.5}$ /SiO_2[24]	20:1	60000	300	97	75	-

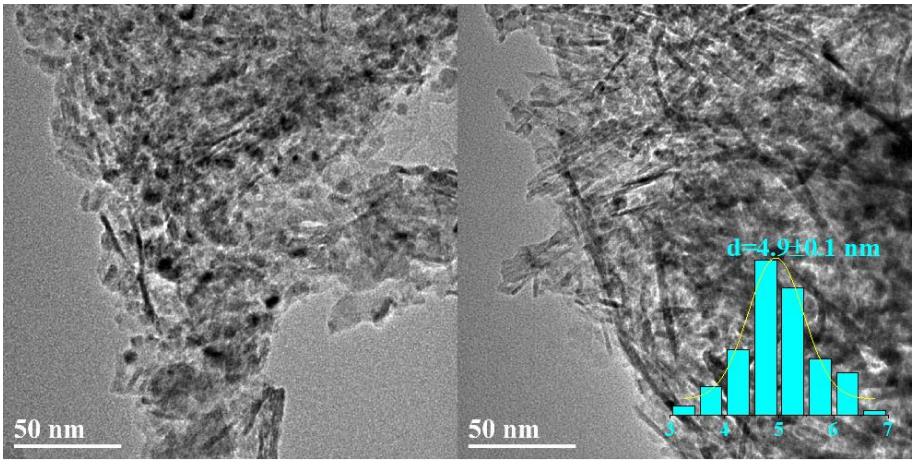

Figure S18 HRTEM images of spent Ni-Cu/r-Al_2O_3 catalyst and the distribution of particle size

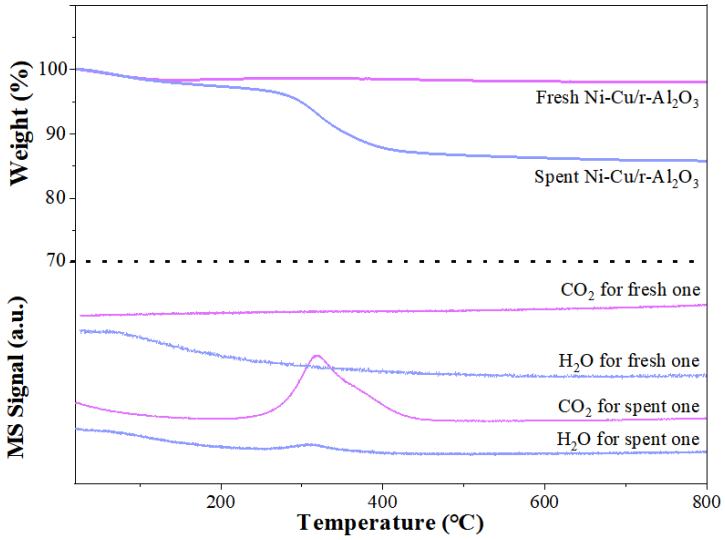

Figure S19 TG-MS analysis of fresh and spent Ni-Cu/r-Al_2O_3 catalysts

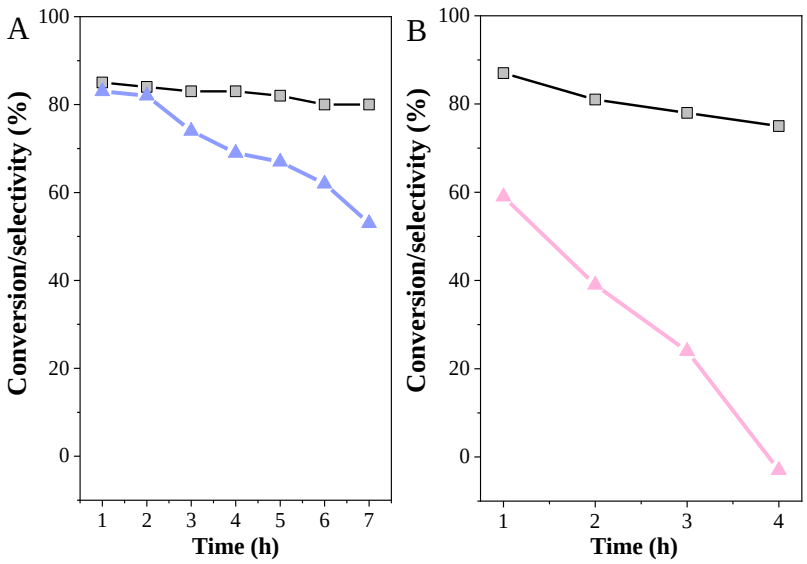

Figure S20 Longer term stability at similar acetylene conversion for (A) Ni-Cu/sp-Al_2O_3 for 7 h (B) Ni-Cu/sh-Al_2O_3 for 4 h (0.3 g of catalyst, 10:1 of H_2/C_2H_2 ratio, total flow = 163 mL min^{-1}, SV = 9780 h^{-1}).

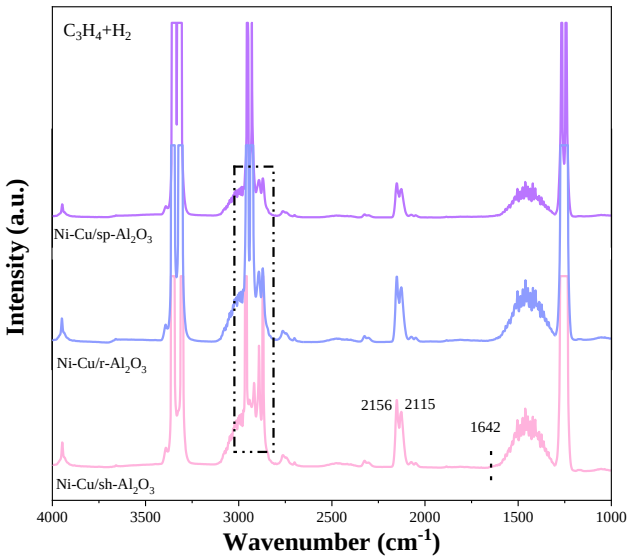

Figure S21 In situ DRIFT spectra with a flow of propyne/hydrogen mixture at room temperatures on nanoshaped Ni-Cu/Al_2O_3

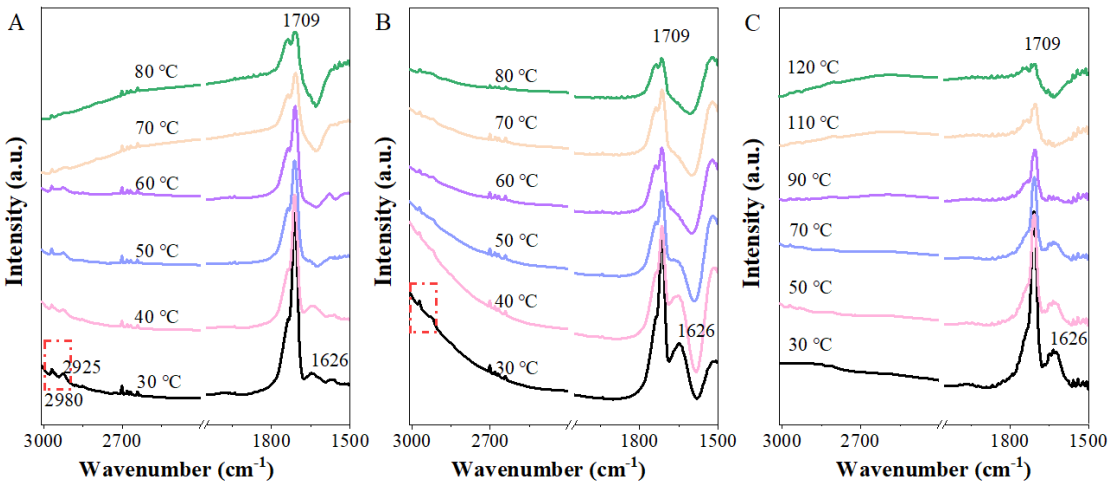

Figure S22 In situ DRIFT spectra of acetylene/hydrogen mixture heated to different temperatures on (A) Ni-Cu/sh-Al_2O_3, (B) Ni-Cu/sp-Al_2O_3 and (C) Ni-Cu/r-Al_2O_3

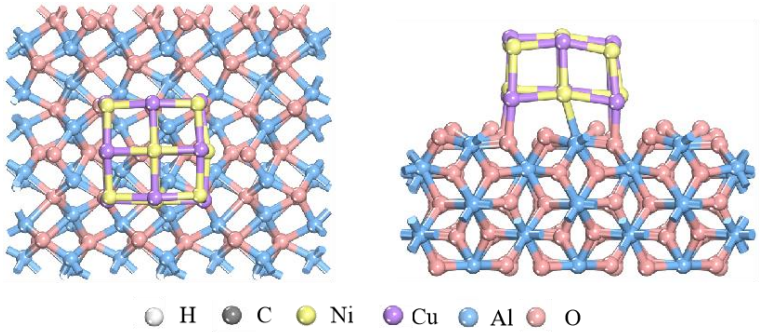

Figure S23 The structures model of Al_2O_3 with exposing (100) facet supported Ni-Cu alloy catalyst

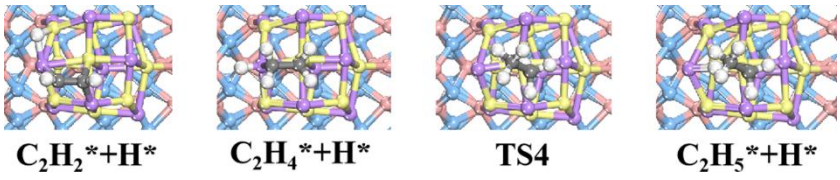

Figure S24 Structures model of the intermediates generated in the process of acetylene hydrogenation over Ni-Cu/r-Al_2O_3

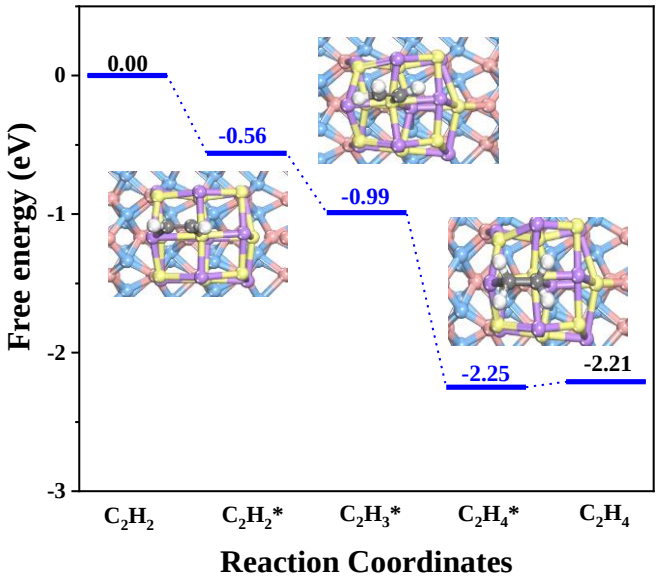

Figure S25 Gibbs free energy diagrams for acetylene hydrogenation on Ni-Cu/r-Al_2O_3

References

[1] Ma, M.; Zhu, Y.; Xu, Z. A New Route to Synthesis of γ-alumina Nanorods. *Mater. Lett*. **2007**, *61*, 1812-1815.

[2] Guo, M.; Shen, Z.; Ling, F.; Yang, W.; Guo, C.; Ji, H.; Hu, Q. Synthesis and Characterization of Nano-sized γ-Al_2O_3 with High Index Surface Planes. *Contemp Chem Ind.* **2015**, *44*, 951-954.

[3] Feng, H.; Wang, H.; Ma, Z.; Wang, S.; Li, P. Quantification of Surface Orientation Effect on the Thermal Stability of γ-Al_2O_3 with Different Morphologies. *Appl. Surf. Sci*. **2022**, *594*, 153509.

[4] Kresse, G.; Furthmüller, J. Efficiency of Ab-initio Total Energy Calculations for Metals and Semiconductors Using a Plane-wave Basis Set. *Comput. Mater. Sci*. **1996**, *1*, 15-50.

[5] Kresse, G.; Furthmüller, J. Efficient Iterative Schemes for Ab Initio Total-Energy Calculations Using a Plane-Wave Basis Set. *Phys. Rev. B.* **1966**, *16*, 11169-11186.

[6] Perdew, J. P.; Burke, K. Ernzerhof, M. Generalized Gradient Approximation Made Simple. *Phys. Rev. Lett*. **1996**, *18*, 3865-3868.

[7] Monkhorst, H. J.; Pack, J. D. Special Points for Brillouin-Zone Integrations. *Phys. Rev. B.* 1976, *13*, 5188-5192.

[8] Blöchl, P. E. Projector Augmented-Wave Method. *Phys. Rev. B*. **1994**, *50*, 17953-17979.

[9] Grimme, S.; Antony, J.; Ehrlich, S.; Krieg, H. A Consistent and Accurate ab Initio Parametrization of Density Functional Dispersion Correction (DFT-D) for the 94 Elements. *J.*

Chem. Phys. **2010**, *132*,154104.

[10] Henkelman, G.; Uberuaga, B. P.; Jónsson, H. Improved Tangent Estimate in the Nudged Elastic Band Method for Finding Minimum Energy Paths and Saddle Points. *J. Chem. Phys*. **2000**, *113*, 9901-9904.

[11] Bergeret, G.; Gallezot, P.; Ertl, G.; Knozinger, H.; Weitkamp, J. Handbook of Heterogeneous Catalysis. **1997**, *2*, 439.

[12] Rossmeisl, J.; Logadottir, A.; Nørskov, J. K. Electrolysis of Water on (Oxidized) Metal Surfaces. *Chem. Phys.* **2005**, *319*, 178-184.

[13] Peterson, A. A.; Abild-Pedersen, A.; Studt, F.; Rossmeisl, J.; Nørskov, J. K. How Copper Catalyzes the Electroreduction of Carbon Dioxide into Hydrocarbon Fuels. *Energy Environ. Sci.* **2010**, *3*, 1311-1315.

[14] Wang, L.; Li, F.; Chen, Y.; Chen, J. Selective Hydrogenation of Acetylene on SiO_2-Supported Ni-Ga Alloy and Intermetallic Compound. *J. Energy Chem.* **2019**, *29*, 40-49.

[15] Chai, M.; Liu, X.; Li, L. SiO_2-Supported Au-Ni Bimetallic Catalyst for the Selective Hydrogenation of Acetylene. *Chinese J. Catal.* **2017**, *38*, 1338-1346.

[16] Boudjahem, A. G.; Chettibi, M.; Monteverdi, S.; Bettahar, M. M. Acetylene Hydrogenation over Ni-Cu Nanoparticles Supported on Silica Prepared by Aqueous Hydrazine Reduction. *J. Nanosci. Nanotechnol*. **2009,** *9,* 3546-3554.

[17] Pei, G.; Liu, X.; Wang, A.; Su, Y.; Li, L.; Zhang, L. Selective Hydrogenation of Acetylene in an Ethylene-Rich Stream over Silica Supported Ag-Ni Bimetallic Catalysts. *Appl. Catal. A*. **2017,** *545*, 90-96.

[18] Fu, B.; McCue, J. A.; Liu, Y.; Weng, S.; Song, Y.; He, Y.; Feng, J.; Li, D. Highly Selective and Stable Isolated Non-Noble Metal Atom Catalysts for Selective Hydrogenation of Acetylene. *ACS Catal*. **2022**, *12*, 607-617.

[19] Simanullang, W.; Ma, J.; Shimizu, K.; Furukawa, S. Silica-Decorated Ni-Zn Alloy as a Highly Active and Selective Catalyst for Acetylene Semi-Hydrogenation. *Catal. Sci. Technol.* **2021,** *11*, 4016-4020.

[20] Chen, Y.; Chen, J. Selective Hydrogenation of Acetylene on SiO_2 Supported Ni-In Bimetallic Catalysts: Promotional Effect of In. *Appl. Surf. Sci.* **2016**, *387*, 16-27.

[21] Riley, C.; Riva, A. D. L.; Zhou, S. Synthesis of Nickel-Doped Ceria Catalysts for Selective Acetylene Hydrogenation. *ChemCatChem.* **2019**, *11*, 1526-1533.

[22] Liu, Y.; Zhao, J.; Feng, J.; He, Y.; Du, Y.; Li, D. Layered Double Hydroxide-Derived Ni-Cu Nanoalloy Catalysts for Semi-Hydrogenation of Alkynes: Improvement of Selectivity and Anti-Coking Ability Via Alloying of Ni and Cu. *J. Catal.* **2018**, *359*, 251-260.

[23] Li, Q.; Wang, Y.; Skoptsov, G.; Hu, J. Selective Hydrogenation of Acetylene to Ethylene over Bimetallic Catalysts. *Ind. Eng. Chem. Res.* **2019**, *58*, 20620-20629.

[24] Liu, H.; Chai, M.; Pei, G.; Liu, X.; Li, L.; Kang, L.; Wang, A.; Zhang, T. Effect of IB-Metal on Ni/SiO_2 Catalyst for Selective Hydrogenation of Acetylene. *Chinese J. Catal.* **2020**, *41*, 1099-1108.